New Considerations for Compact Cyclotrons
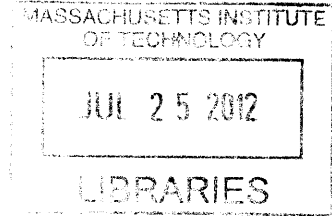
by

Eric S. Marshall
B.S., Physics
U.S. Air Force Academy, 2002

SUBMITTED TO THE DEPARTMENT OF NUCLEAR SCIENCE AND
ENGINEERING IN PARTIAL FULFILLMENT OF THE REQUIREMENTS FOR
THE DEGREE OF

MASTER OF SCIENCE IN NUCLEAR SCIENCE AND ENGINEERING
at the
MASSACHUSETTS INSTITUTE OF TECHNOLOGY

JUNE 2012

Signature of Author: ....
Department of Nuclear Science and Engineering
May 5, 2012

Certified by: ....
Richard C. Lanza
Senior Research Scientist
Thesis Supervisor

Certified By: ....
Dennis G. Whyte
Professor of Nuclear Science and Engineering
Thesis Reader

Accepted by: ....
Mujid S. Kazimi
Chair, Department Committee on Graduate Students

New Considerations for Compact Cyclotrons

by

Eric S. Marshall

Submitted to the Department of Nuclear Science and Engineering
on May 5, 2012, in partial fulfillment of the
requirements for the degree of
Master of Science in Nuclear Science and Engineering

Abstract

A compact cyclotron built with superconducting magnets could be a transformative solution to many scientific problems facing the defense, medical, and energy industries today. This thesis discusses three potential applications of compact cyclotrons: generation of ^{13}N for medical imaging, active interrogation for counter-proliferation, and fast neutron imaging for Enhanced Stockpile Surveillance (ESS). The first two applications are broadly reviewed. The ESS imaging application extends from preliminary work performed by Lawrence Livermore National Laboratory, who proposed a linear accelerator-driven ^{2}H(d,n)^{3}He reaction, and a complex gas-handling target subsystem. Here, the entire source-side engineering is reconsidered by investigating the viability of 56 different neutron-producing reactions. It is found through Monte Carlo simulation that the ^{7}Li(p,n)^{7}Be reaction could improve image contrast by employing a superconducting cyclotron capable of 3.8 MeV, 414 μA proton beam and liquid lithium target.

Thesis Supervisor: Richard C. Lanza

Title: Senior Research Scientist

Thesis Reader: Dennis G. Whyte

Title: Professor of Nuclear Science and Engineering

Acknowledgments

It has been said that undergraduates want to think they know everything, Masters students learn that they know nothing, and PhD's learn that nobody knows anything. In spite of how accurately that applies to my academic experience, I am very grateful to some folks who were integral to my curricular and research endeavors. I thank...

Dr Lanza, for expanding my mind on every topic under the sun, for allowing me the space and latitude to follow my curiosities, and for tasking me to use a table saw and Ramset all summer in the name of science.

Dr Antaya, for an exceptional draft review and sharpening my understanding of cyclotrons.

Fellow travelers—Chad, Chris, Mareena, Zach, Brittany, Brandon, Harold, An, Tyrell & Tyler (Go Army, Beat Navy), Alex and Shawn.

Carl and Henry, for the dislocated rib, sore muscles, and the weekly chance to be a Soldier.

West Point's Physics and Nuclear Engineering department, for investing in my education and giving me a chance to do what I've always wanted to do.

Drop Kick Murphys, for the music. Anna's Tacqueria, for the burritos.

The bear in the Pemigewasset Wilderness, for not eating Andy and I that night last October. You changed my outlook on things, and this thesis is much better because of your restraint.

Ali, for the wonderful ten years. Glory and Asa, for being cute and enjoying rope swings as much as I do.

Contents

List of Figures

List of Tables

1 Introduction

A compact cyclotron built with superconducting magnets could be a transformative solution to many scientific problems facing the defense, medical, and energy industries today. Though the fundamental physics of cyclotrons was solved decades ago, they have not yet been widely adopted. The size, beam current, and energy range of compact cyclotrons make possible new nuclear reactions and mission sets, which affect market and defense decisions. The common thread uniting the project work and independent study that I have engaged in at MIT over the past two years is an appreciation for the unrealized potential of compact cyclotrons. This thesis summarizes three specific applications, their possibilities and limitations.

Isotope generation for radiotherapy is not a new application for cyclotrons, but a first-of-its-kind device is described whose wall-powered 6 T magnetic field reduces its overall footprint to almost half that of its competitors. Large linear accelerators are not necessary to drive ion beams for the interrogation of cargo in search for smuggled nuclear material: a superconducting cyclotron the size of a trash can may be able to generate a secondary beam of gamma rays, delivering higher average current and less unnecessary dose in a much smaller frame. These two concepts are described in Chapter 2.

In Chapter 3 a fast neutron imaging system is described for the Enhanced Stockpile Surveillance Program using the ^{2}H(d,n)^{3}He reaction and a radio-frequency quadrupole LINAC. Special emphasis is placed in this thesis on systematically investigating 56 other potential reactions that are made feasible by the accelerating gradient

of compact cyclotrons. After evaluating engineering tradeoffs, I recommend that the project team consider the ^{7}Li(p,n)^{7}Be reaction with a liquid jet target and superconducting cyclotron as a feasible alternative to the source-side technology approach. Chapter 4 concludes with thoughts on common themes emerging from the study of the three applications.

The remainder of this chapter provides context by discussing the historical setting in which accelerators arise. Some may wonder, with benefits so apparent and physics so accessible, why has the adoption of compact cyclotrons been so limited? This review is followed by a brief synopsis of the salient physics of accelerators and recent technological developments that motivate a fresh look at old problems.

1.1 A Historical Perspective

Particle accelerators have been used in research labs for over eight decades, but their broader adoption in society has occurred only recently. In 1928 R. Wideröe reported the first operation of a 25 kV linear accelerator with potassium and sodium ions. E. O. Lawrence read Wideröe's paper in 1929 and built his own LINAC in 1931, accelerating mercury ions to 1,000 kV. Seeking higher energies without increasingly longer vacuum cylinders, Lawrence conceived of the cyclotron. His design for an 80 keV cyclotron was patented in 1931. The next year he and Stanley Livingston achieved 1.1 MeV in an 11-inch machine. That same year, in 1932, John D. Cockroft and Ernest Walton used protons to split a lithium nucleus into two alpha particles, causing the first artificial nuclear reaction. They multiplied a 200 kV transformer's potential to 800 kV by mechanically opening and closing switches to an intricate stack of capacitors and diodes.

The utility of particle accelerators for exploring the atomic nucleus was quickly recognized. In the early years, x-ray radiography for medical purposes and breeding fuel for nuclear weapons were fashionable and lucrative research areas. Thus, accelera-

14

tors benefited from a frenzy of financial and intellectual investment. By the mid-fifties practically all of the physics problems were solved with regard to radiofrequency structures and beam dynamics.

For fifty years, then, the development of particle accelerators progressed in the realm of nuclear and high energy particle physics, yet their contribution to everyday life stagnated (perhaps with the exception of the cathode ray tube). A German physicist visiting the US in Lawrence's day noted, "Americans seem to work very well, only they obviously insist on making everything as big as possible."[1] Both the interest of researchers and funding in the basic sciences went headlong into probing the inner workings and architecture of the nucleus with enormous synchrotrons and storage rings, increasing the ion energy by a factor of 10 every 6-8 years [2].

Some accelerator applications, such as cathode ray tubes and x-ray radiography, flourished, but societal adoption of ion accelerators in the modest energy range of 5-30 MeV for applications like medicine, security, and sterilization was slow. As a case in point, the U.S. is still dependent on foreign reactor-based ^{99}Mo for radiotherapy, though accelerators are clearly up to the task. Ironically, even Lawrence conducted experiments with his primitive cyclotrons to generate radioisotopes for medical purposes.

Today particle accelerators are frequently seen as the inevitable tools for solving current scientific problems. The US DOE's *Accelerators for America's Future* discusses how useful a beam of particles can be:

> A beam of the right particles with the right energy at the right intensity
> can shrink a tumor, produce cleaner energy, spot suspicious cargo, make
> a better radial tire, clean up dirty drinking water, map a protein, study
> a nuclear explosion, design a new drug, make a heat-resistant automotive
> cable, diagnose a disease, reduce nuclear waste, detect an art forgery, im-
> plant ions in a semiconductor, prospect for oil, date an archaeological find,

---

[1] Quote by Franz Simon in 1932 [1].

package a Thanksgiving turkey or discover the secrets of the universe [3].

Nevertheless, according to the DOE report, bridging the "valley of death" between laboratory proof-of-principles and the production line remains a formidable challenge. New accelerator applications often require significant improvements in "traditional" accelerator output beam properties, including higher beam currents, lower angular divergence, and lower cross sectional area. At the same time, it may be necessary to achieve smaller energy spread, shorter bunch length, and improved extraction efficiency. The US lags behind many other countries that are promoting these new accelerator technologies more determinedly, e.g. Belgium, China, Poland, Japan, and Germany [3].

The scale of the future benefits of these new accelerator technologies may be imagined by considering the economic impact of the traditional accelerators today. There are about 30,000 particle accelerators operating in the world today. The market value of medical and industrial accelerators alone exceeds $3.5 billion, and this number is growing at a rate of more than 10% annually [3].

Something must *transform* the pace of accelerator development to attain the new beam requirements for solving current problems. What are the drawbacks or tradeoffs to achieving the necessary beam? It is unlikely to be a limitation of physics. Most often, practical constraints that can be correlated to financial costs preclude private investment in many scientific problems: in the case of accelerators these constraints are footprint and input power. The next section presents the accelerating gradient as the driving parameter that determines the feasibility of an accelerator to deliver the necessary particle beam.

1.2 Motivation: the Accelerating Gradient

The convergence of several significant technological advancements that together serve to make cyclotrons *smaller* may make the difference in the U.S. and abroad. The DOE

16

report emphasizes the advantages of the compactness of new accelerators. In general, physically smaller devices are friendlier to the industrial sector that will manufacture and transport them, resulting in lower unit cost. The smaller size also improves market access in areas where footprint and input power are mission or economic imperatives. At this point the futures of LINACs and cyclotrons diverge, so we follow with separate descriptions of drift tube linear accelerators (DTL), radio-frequency quadrupoles (RFQ), and cyclotrons.

Drift Tube Linear Accelerator

DTLs are LINACs that accelerate particles by applying an alternating electric potential in exactly the proper sequence to move a particle along a hollow tube. At the tube entrance the field accepts the particle with a sign opposite the charge of the particle. As the particles drift, the phase of the electric field is changed, and, at the exit of the tube, the particle is accelerated with a push from the field. For a given beam energy, the higher the frequency of the alternating field, the shorter the drift tubes and, hence, the entire system. Since the particles must traverse the length of one drift tube in one cycle of the electric field, the length of the drift tube must be

$$l = \beta \lambda_o, \tag{1.2.1}$$

where β is the fraction of the speed of light for the particle, and λ_o is the free-space wavelength of the radiofrequency signal.

Physicist J. C. Slater showed in 1947 that the input power per unit length in a DTL is proportional to (among other factors) the wavelength:

$$P_l = \frac{A \, \epsilon_o \, E_l^2 \, \lambda_o^2 \, \omega_o}{Q}, \tag{1.2.2}$$

where A is a constant related to the field distribution, ϵ_o is the permittivity of free

space ($c = 1/\sqrt{\epsilon_o\,\mu_o}$), E_l is the accelerating voltage per unit length, ω_o is equal to $2\,\pi\,c/\lambda_o$, and Q is a loss factor inversely related to the dissipation of power into the walls of the machine (the greater the power dissipation, the smaller the Q) [4]. It is essential, therefore, that wavelengths be kept small. Radiofrequency (RF) structures of 200-500 MHz are typically used.

By rewriting Equation 1.2.2 for total input power P (rather than power per unit length) and final ion energy T we see that power is proportional to the total acceleration *squared*, and inversely proportional to the total length:

$$P = C\,\frac{T^2\,\sqrt{\lambda_o}}{l}, \tag{1.2.3}$$

where $C = 2\,\pi\,A/Q\,\sqrt{\epsilon_o/\mu_o}$, a constant dependent on the geometry of the system [5]. Any amount of acceleration can be attained from a fixed power source by making the DTL indefinitely long. Likewise, a DTL may be shortened, provided the final ion energy is nominal or the power to the system is substantial.

The DTL is widely used because of its ability to generate high-current, high-quality beams with an increasingly high duty factor (ratio of the duration of the beam to the period of the RF). Also, the DTL has distinct advantages because of the ease of injecting the beams to be accelerated and the ease and high efficiency of extracting the final accelerated beam. When using a DTL, the primary tradeoff identified by Equation 1.2.3 is length.

Reasonably sized DTLs must have power amplifiers that can provide high power at high frequency. These have only recently become available in the form of klystrons, which provide pulsed power that reinforces the *bunching* of ions in the drift tubes. The inherent pulsed beam of DTLs can equate to very high peak currents (easily above 10 mA), but the time averaged current is on the order of a couple hundred microamps.

18

Radiofrequency Quadrupole Linear Accelerator

The RFQ is a relatively new type of LINAC that is especially designed for the acceleration of low-velocity ion beams. The RFQ does not strictly follow the scaling relationships in Equation 1.2.3, and its utility as a stand-alone accelerator is limited. It is typically used as an injector for high-energy systems.

DTLs are limited to low current due to focusing deficiencies at low energies. In all ion LINACs the longitudinal effects of space-charge repulsion are counteracted by phase focusing in the accelerating gap, and the bunched character of the beam is maintained. The use of phase focusing inherently produces transverse defocusing forces that must be counteracted by extrinsic means. These defocusing forces have greater strength for low-velocity ions, so space charge repulsion is more prominent at low velocities. For high-current beams, nonlinear space charge forces will rapidly and irreversibly cause transverse emittance growth [6].

RFQs are different from DTLs because they simultaneously focus and accelerate the ions with the velocity-independent electric field force. The four pole tips are copper vanes, precisely crenelated to the shape of the RFQ potential function. The RFQ easily accepts the ions from a low voltage injector, focuses, bunches, and accelerates the ions to a velocity where the DTL has sufficient current capacity to accelerate the ions further [6].

There are other techniques, in addition to the RFQ, for augmenting the energetic range of a LINAC. Most of the techniques are captured by the constant C of Equation 1.2.3: improve conductivity, reduce power dissipation through walls, and improve cavity geometry. For instance, magnetic quadrupole focusing introduces a velocity-dependent focusing force to reduce beam loss. That design is common now, but mostly improves beam current capacity at higher velocities.

We will assume for scaling and comparison purposes that Equation 1.2.3 is sufficiently accurate, despite recent advancements in LINAC technologies. The most

important parameter for accelerator applications will always be the final ion energy. RF structures are practically limited to 1.25 GHz. After these, the beam energy and system length tradeoff is unavoidable. As Slater put it, "There seems to be no scientific way of deciding what separate values of power and length to use, and therefore the decision will presumably be based on economic arguments" [4].

Cyclotron

Cyclotrons achieve higher beam energies in much smaller footprints by using a magnetic field to bend the ions into circular orbits. As in a LINAC, particles are accelerated in gaps between conductive *dees* where an electric field alternates sinusoidally, but in a circular machine they pass through the same gap many times. In classic or isochronous cyclotrons the gap voltage remains constant, and particles are grouped into beam *envelopes* according to their turn radius, which is a function of their kinetic energy for that turn:

$$r_g = \frac{m\,v}{q\,B(r)}, \tag{1.2.4}$$

where r_g is the *gyroradius*, m/q is the ion mass-to-charge ratio, and $B(r)$ is the axial magnetic field at radius r. This is derived directly from the Lorentz Force Law. The increase in gyroradius is analogous to the increase in drift tube length for the linear machine. When the particles reach the maximum dee radius, the beam extracts as a continuous wave rather than a pulse.

One criterion useful in comparing circular and linear accelerators is the accelerating gradient—the energy gain per length of the machine. This is the same as E_l defined in Equation 1.2.2. The cost of many accelerator components is linearly proportional to the length of the beam line. If we take, for example, the CYCLONE 18/9 built by IBA Molecular, it can produce 150 μA of 9 MeV deuterons in a 2 m diameter frame. Dividing the energy by the circumference of the final orbit ($r \approx 0.5$ m) gives an effective gradient exceeding 2.8 MV/m. A comparable LINAC design proposed by

AccSys Technology is 5 m long and produces the same average current of 7 MeV deuterons [7]. Its accelerating gradient is 1.41 MV/m. The two-fold difference in E_l is significant. One also notes, however, that the peak input power for the cyclotron is 50 kW, while the peak power requirement for the LINAC is almost 550 kW. The former requires a specialized circuit, the latter a bank of high voltage transformers.

By maximizing the accelerating gradient, cyclotrons that employ superconducting magnets could be a transformative technology where input power and footprint are constrained. Like LINACs, conventional cyclotrons utilizing resistive magnets lose power due to ohmic heating ($P = I^2R$). Superconductors are insulated in a cryogenic vacuum, and therefore have no DC electrical power losses.

A cyclotron's system size is determined by the pole radius of the cylindrical magnet that guides the particles. Rewriting Equation 1.2.4 we get[8]:

$$r^2 = \frac{2\,T\,m}{q^2\,\bar{B}^2} \quad \text{or} \quad T \approx 48\,\text{MeV}\,r^2\bar{B}^2. \tag{1.2.5}$$

The superconducting IBA C250 has a magnet field of 4 T and a pole radius of 0.9 m. With an input power of 190 kW it can accelerate protons to 250 MeV [9], resulting in an accelerating gradient of 44.2 MV/m. By comparison, the Canadian Light Source injector LINAC achieves 250 MeV with six klystrons inputting 20 MW of power each. Despite the generous power load, the total length of the machine is 24 m long [10], with an effective accelerating gradient of 10.4 MV/m.

Superconducting cyclotrons can be applied beneficially in lower energy regimes as well. One model under development, and discussed in Section 2.1, will enable the in situ generation of the radioisotope ^{13}N with 12.5 MeV protons. The expected 6 T average magnetic field of the cyclotron makes it much more compact than resistive magnet competitors. Its isochronicity—a radially variant magnetic field usually used to offset relativistic effects—enables this nonrelativistic beam to achieve the desired final energy in *more* turns. More gap crossings means that less voltage is needed to

accelerate the ions to higher orbits. Consequently, the entire system can run off of hospital wall power.

Superconducting coils and isochronous magnet topologies are not new to the research communities, but their successful implementation to meet market demands is. Scientists solved many of the field design and beam extraction problems associated with compact cyclotrons in the 1980's. To get beyond the lab, auxiliary systems needed to be refined, such as the cryogenics to keep the superconductors near 4 K and the ion injection system to initiate the ions with enough energy to avoid phase space and resonance problems. A major hurdle in cyclotron design is controlling beam emittance: resonances, field aberrations, and inherent phase instability cause beam loss into internal components that reduces current and activates the machine. High precision beam modeling and simulation programs, along with virtual prototyping, reduce some of the uncertainty associated with the capital costs to build the devices. [2]

Innovations continue to propel the compact cyclotron forward through the "valley of death" to new and useful applications. Cyclotrons need to be lighter and more mobile for some security and industrial uses. They may continue to shrink as the superconductor industry finds ways to engineer the brittle Nb_3Sn conductor, which is capable of three times the current density of conventional NbTi at the same temperature [11]. High intensity beams $\sim$10 mA would be useful for long stand-off nuclear material detection and for transmutation of nuclear waste. Increasing the current and final energy to GeV regimes means continuing to improve extraction efficiency, real-time beam diagnostics and correction, and ion injection systems.

---

[2]For an example, see Mingwu Fan, et al, "Progress in Virtual Prototyping for Design of Compact Cyclotrons." International Conference on Electrical Machines and Systems, 2008.

2 New Compact Cyclotron Applications

The previous chapter highlighted the accelerating gradient as the salient factor driving the utility of compact cyclotrons. The associated technical hurdles would be most likely overcome in fields where reduction of system size is an explicit criteria. This chapter overviews two such applications for compact cyclotrons: radiopharmaceutical production and detection of smuggled nuclear materials. Aside from economic and public health benefits, these applications are related in that both have nuclear security implications. For each application, the problem background, possible solution, and future work will be discussed.

2.1 Radioisotope Production for Medical Imaging

2.1.1 Background

Nuclear medicine imaging relies on the tracer principle first established in 1913 by George de Hevesy, involving the introduction of small quantities of a radioactive substance into the body. The radioactive material is then distributed, accumulating in particular organs. Today tens of millions of patients receive accelerator-based diagnosis and treatments in hospitals around the world. LINACS or cyclotrons that generate the necessary radiopharmaceuticals weigh many tons and require a reinforced floor to

accommodate them structurally.

Smaller compact cyclotrons would be preferable for their advantageous weight, footprint, and power requirements. Improved economies of scale would make nuclear medicine procedures more widely available, advancing health and quality of life in regions currently without nuclear medicine. One potential application of these smaller superconducting cyclotrons in the medical field is investigated: generation of ^{13}N for myocardial perfusion via Positron Emission Tomography (PET).

Myocardial perfusion is a nuclear medicine technique that images the decay radiation from a radionuclide inserted into the blood stream to diagnose various heart conditions, such as coronary heart disease. Traditionally, the procedure is performed using ^{99m}Tc. This short-lived ($t_{1/2} \approx 6$ hrs) metastable isomer is "milked" from its parent isotope, ^{99}Mo, in a hot cell. The isotope is added to whatever pharmaceutical is being administered to the patient in order to trace its movement through the body. ^{99m}Tc emits a single 140 keV gamma ray to become a stable nucleus. Gamma-cameras obtain 2D images of the 3D distribution of the radionuclide, informing physicians on patients' neural activity or blood flow. This procedure is called Single Photon Emission Computed Tomography (SPECT) and is commonly used for researching pathologies such as dementia and Alzheimer's disease [12], as well as for diagnosing cardiac stress [13].

Using ^{99m}Tc is problematic, however, for several reasons. First, since its parent nuclide ^{99}Mo is formed in special nuclear reactors that irradiate highly enriched uranium (HEU), its use entails all of the problems associated with HEU and spent nuclear fuel: e.g., proliferation risks, security costs, and waste disposal. Secondly, the U.S. is almost completely dependent on foreign companies for its entire supply of ^{99}Mo. ^{99}Mo cannot be made in domestic power reactors because the target requires a completely different technology incompatible with U.S. reactors [14]. Furthermore, because ^{99}Mo has a 66 hr half-life, each imported batch is only good for about a week before it has decayed. Planned or unplanned facility shutdowns, such as that of Canada's National

24

Research University (NRU) reactor at Chalk River in November 2007, can have a devastating effect on provision of care in U.S. hospitals [15]. Thirdly, the generation and extraction of nuclear medicines from reactor products involves a complex manufacturing and supply process. The production and logistical expense results in higher health care costs passed on to patients and tax payers [14]. These concerns have compelled the nuclear medicine industry and U.S. government to develop a domestic capacity in the long run [16, 17, 18]. These efforts are ongoing, but they have significant cost tradeoffs and will not be realized for some time.

An alternative procedure for myocardial perfusion imaging is Positron Emission Tomography (PET), which relies on an altogether different nuclear decay scheme. A positron emits from the unstable parent nucleus and interacts with an electron within ~1 mm of neighboring tissue, annihilating both particles and releasing two 511 keV gammas in opposite directions. The PET scanner ring detects these simultaneous radiations, localizing the source along a straight line of coincidence (LOC). Radionuclides used in this procedure are ^{11}C, ^{13}N, ^{15}O, and, most prominently, ^{18}F. The higher energy gammas yield improved resolution over SPECT, their short half-lives result in lower dose to the patient, and the low-Z nuclides lend themselves to more favorable chemistries for *in vivo* pharmaceutical and diagnosis purposes [19]. A full discussion of the relative advantages and disadvantages of these procedures (SPECT and PET) and all possible nuclides lies outside the scope of this paper. A discussion on the prospects for generating one nuclide, namely ^{13}N, in a superconducting cyclotron follows.

2.1.2 Possible Solution

The radionuclide ^{13}N may be produced in a cyclotron by bombarding a water target with a beam of protons. Figure 2.2.2 (top) shows that the cross section of the reaction ^{16}O(p,α)^{13}N reaction peaks at about 50 mb with 11 MeV protons.
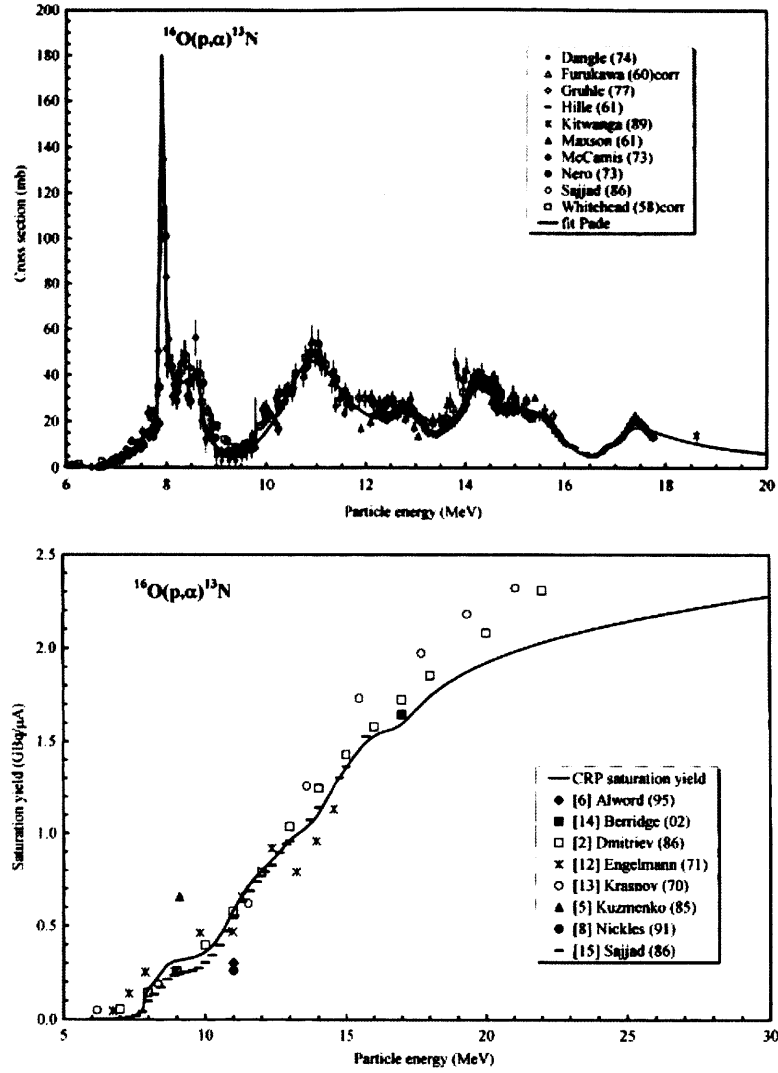
Figure 2.1.1: Cross section (top) and saturation yield (bottom) of $^{16}O(p,\alpha)^{13}N$ reaction. Both plots come from [20].

The ^{13}N begins to decay as soon as it is created while the target continues to undergo irradiation. Hence, when the ratio of the product's half-life to the irradiation time is sufficiently low, the activity of the product is constant for a given beam current. For an 11 MeV beam, Figure 2.1.1 (bottom) shows that the so-called *saturation yield* is about 0.6 GBq/μA, and increases sharply with higher energies. A 12.5 MeV beam yields 0.9 GBq/μA (24.3 mCi/μA). Only 1 μA of 12.5 MeV beam is necessary to

achieve the prescribed dose of 20 mCi for PET imaging [21]. The accelerator current and the volumetric flow rate of the target apparatus could conceivably be much higher.

The difficulty of using N-13 is that it has a half-life of 10 minutes, so it must be made locally. The accelerator would need to be very compact due to the limited space for equipment and shielding in a clinical setting. Ideally, it would be near the patient and run off of normal wall power. Figure 2.1.2 below depicts such a configuration.
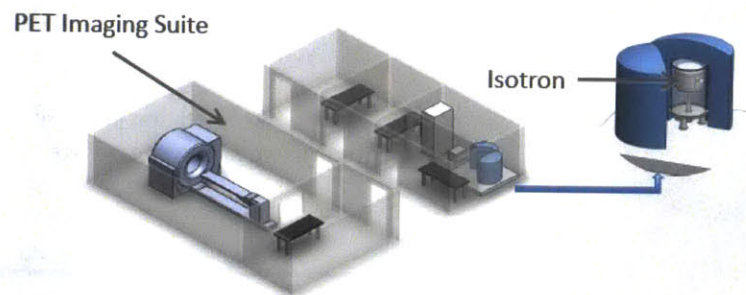
Figure 2.1.2: Particle accelerator in a clinical setting. The human resource, environmental and space constraints require that the cyclotron—here called an ISOTRON—be low-maintenance, self-shielding, and compact. Image used by permission of Ionetix Corporation.

The proximity of the equipment to patients mandates the machine be self-shielding: all lost beam must be attenuated in the steel yoke around the magnet. A 95% beam extraction rate is desired.

2.1.3 Future Work

A prototype cyclotron expected to meet these specifications has been developed by IONETIX CORPORATION. Its operating parameters are listed in Table 2.1.

Table 2.1: USIC operating parameters with isometric view of prototype
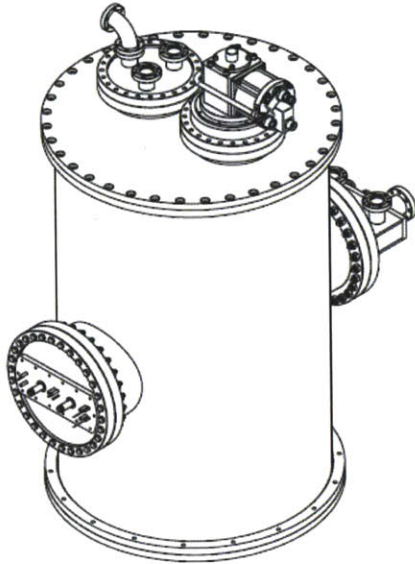
Magnetic field (T)	6.08	
Max average current (μA)	100	
Nominal average current (μA)	1	
Period width (nsec)	10.7	
Beam width (nsec)	1.1	
Wall power (kW)	6	
Height (cm)	100	
Diameter (cm)	60	
Mass (kg)	454	
Operating temperature (K)	4-5	
Conductor	NbTi	
Accelerated particle	p^+	d^+
Cyclotron frequency (MHz)	93.38	46.69
RF frequency (MHz)	93.4	93.4
Acceleration harmonic	1	2
Final ion energy, maximum (MeV)	12.5	6.25
Target material[†]	^{16}O	^{11}B
Target yield	^{13}N	^{12}C
Radiations produced	α, γ	n, γ

A Nuclear Science and Technology research team at MIT has collaborated with IONETIX to test this Ultracompact Superconducting Isochronous Cyclotron (USIC), characterize its intrinsic radiation field, and measure the activity of ^{13}N it produces.

USIC has several unique characteristics that make it a first-of-its-kind device. First, its superconducting niobium-titanium magnet coils are expected to hold a field of 6 T. Per Equation 1.2.5, this scales the magnet pole tips to 1/4 that of existing compact cyclotrons, for a given final proton energy, operating with resistive magnets at 1.5 T. Indeed, the total system diameter of IBA's CYCLONE 11 is 3.66 m.[1] The USIC should be less than 1 m. The commercial version is expected to be significantly smaller.

Secondly, the USIC magnet is isochronous—the axial field is designed to increase with increasing radius. Typically isochronicity is employed to offset the effects of relativistic mass increase. In USIC, the protons do not approach transition energies,

---

[1]These technical specifications and others for the IBA products mentioned in this thesis may be found at www.iba-cyclotron-solutions.com/products-cyclo.

but increasing the field at larger radius increases the frequency of rotation. Increasing the gyrofrequency increases the RF frequency, and it decreases the peak RF voltage. The particles accelerate less each time they cross a dee gap, but they undergo more revolutions inside the cyclotron. Less input power is required to achieve the same final energy. USIC runs off of 220 V / 30 A wall power.

The collaboration between MIT and IONETIX must proceed on USIC to clarify three areas of uncertainty. First and foremost, the machine must be completed and tested to determine as-built operating parameters. Quantities of interest are the vacuum efficiency and insulation of the cryostat, the magnet field with respect to radius, beam extraction efficiency, emittance, and functionality of all appurtenances and instrumentation (these include the ion source, PLC, RF system, and cryo-compressor).

Second, the production of ^{13}N must be measured, as well as the associated radiation field. In-stream activity measurement of a positron emitter is not straightforward. In fact, the quality control of PET isotope generation in compliance with FDA purity standards is one major factor keeping PET from replacing SPECT using the relatively inexpensive ^{99}Mo. Moreover, the inelastic scatter cross section is high for ^{16}O(p,p'γ). Activated ^{16}O de-excites with four discrete gamma lines ranging from 2.7 to 7.1 MeV [22]. The unique radiation field from USIC operation must be characterized empirically in order that sufficient shielding will be incorporated in the commercial version.

Finally, the cyclotron operating parameters and target chemistry must be optimized to achieve maximum and FDA-compliant ^{13}N production. Production efficiency is paramount to overcoming the barriers to market entry set by SPECT tracer modalities. Though one study found that PET and SPECT imaging methods are not in direct competition, PET inherently requires a more sophisticated clinical infrastructure to administer (even in the form of a very compact cyclotron) [23]. One way for a PET tracer to compensate for that disadvantage, which is fundamentally an economic factor, is by fine-tuning the target chemistry. It is known that adding methane (CH_4)

to the water target increases the production of ^{13}N-ammonia (NH$_3$) [24]. Ammonia is the desired chemical form for administering the radioisotope into the body. It is not well known what the pressure of the methane should be, how much head space should be afforded for gassification in the target, and how much heat will be created that could lead to phase-change and other problems. These unknowns must be investigated empirically.

2.2 Active Interrogation for Counter-Proliferation

2.2.1 Background

National security agencies are increasingly concerned with the illicit transfer of nuclear weapons, improvised nuclear devices (IND), or special nuclear material (SNM) by state and non-state entities. The International Atomic Energy Agency establishes assurance and deterrence through International Safeguards. Other multilateral agreements, such as the Proliferation Security Initiative, give states the authority to interdict when transfer is known to occur. In both cases, verification of illicit transfer begins with timely detection of a significant quantity of SNM.

Once diverted from its point of origin, WMD or SNM detection is performed by either passive or active interrogation. Passive detection looks for the 186 keV gamma decay line in ^{235}U and the 2.60 MeV line in the ^{208}Tl impurity. This is very difficult in practice because both signatures are easily shielded or are otherwise indiscernible from background [25].

Active interrogation, on the other hand, induces fission in the SNM, yielding highly penetrative radiation that cannot be easily shielded. Detecting this signal could lead to the interdiction of a nuclear weapon or IND before it arrives at its intended destination. The broader adoption of active interrogation capabilities would confront our enemies with more risk in their choice of diversion and deployment pathways.

Active interrogation using either photons or neutrons induces fission in the shielded HEU or Pu, and a variety of prompt and delayed ($>10^{-14}$ sec) radiation is produced. Prompt emissions of neutrons and gammas from the fission of actinides have known fluctuation distributions that deviate from typical Poisson statistics in a time interval after interrogation. These deviations distinguish the presence of SNM from other material activated by the beam in the vicinity of the target because fission produces higher multiples of coincident counts. A pulsed beam, i.e. a LINAC, is required for this interrogation/detection scheme so that detection can occur between the pulses [26].

A LINAC-based system has limited utility, however, due to the size of the accelerator and associated pulsed power sources needed to produce a beam of the right energy. Compact cyclotrons, on the other hand, are suitable for any number of environments where footprint must be limited and power supply is scarce. Since cyclotrons emit continuous waves (CW), not pulsed beams, a different detection mode must be employed.

2.2.2 Possible Solution

The Secondary Gamma Beam

The key to using a CW accelerator is detecting the *delayed* radiation resulting from the induced photofission. After the initial photofission, additional fissions in the HEU are caused by the chain multiplication processes. Though they are fewer in number, delayed neutrons are more likely to induce fission due to the higher cross section of ^{235}U for thermal neutrons. The time dependence of subsequent radiation has been thoroughly measured and found to be directly proportional to the prompt radiation [26].[2] Thus, detection of the delayed emissions can identify SNM, is discernible from

---

[2]For delayed neutron yield see G. R. Keepin, T. F. Wimmett, and R. K. Zeigler, R. K. *Physics*, 107, 1044 (1957) . For delayed gamma yield see José March-Leuba, J. K. Mattingly, J. A. Mullens, T. E. Valentine, J. T. Mihalczo, and R.B. Perez. "Methodology for Interpretation of Fissile Mass

background (nearby material will not have delayed radiation), and can be measured after the interrogation source is disabled. Consequently, a higher fluence non-pulsed source could be used, increasing the probability of induced fission and detection.

Most viable interrogation sources involve the acceleration of charged particles into a target, which then undergoes a nuclear reaction to generate a secondary beam of interrogating particles. One concept being investigated by MIT's PSFC for the Defense Threat Reduction Agency (DTRA) is a compact cyclotron that accelerates deuterons for the ^{11}B(d,nγ)^{12}C* reaction. The reaction has a 13.7 MeV Q-value, so a 5 MeV deuteron is enough to excite the recoil nucleus, ^{12}C, to its 15.1 MeV energy level. This level's direct-to-ground transition appears with about 7-8% relative emission intensity (see Figure 2.2.1, left). A secondary beam of 15.1 MeV gammas would be ideal for active interrogation, since the actinides are susceptible to photofission around 10 MeV and peak between 14-15 MeV (see Figure 2.2.1, right).
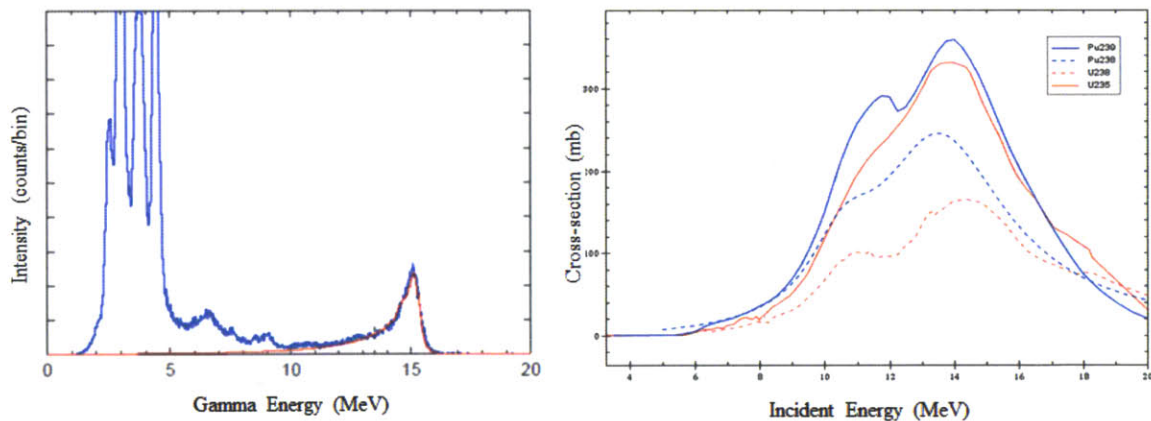
Figure 2.2.1: Intensity of gamma emissions from ^{11}B(d,nγ)^{12}C* reaction (left) [27]. Photofission cross section of select actinides (right) (from ENDF/B-VII.0). The prominent 15.1 MeV gamma line is near the photofission peak energy.

A compact accelerator-based system as described here could be deployed in a variety of scenarios, from port of entry inspections to standoff detection on container-

---

Flow Measurements," *38th Annual Meeting of the Institute of Nuclear Materials Management*, Phoenix, Arizona, July 20, 1997.

ized cargo vessels. One serious disadvantage of active interrogation with the d-^{11}B reaction is the large dose incurred by workers or stowaways from the reaction's associated neutrons, which will be forward-scattered with the secondary gamma beam, and from activation of surrounding material.[3] The next example of active interrogation addresses that problem.

Transmission Radiography

Gamma transmission radiography is a method of detecting SNM by simultaneously imaging and actively interrogating a target with a beam of monoenergetic gamma rays. Radiography is used to locate high-Z material and active photons can identify type and relative quantity of SNM. Imaging is facilitated by pair production in high-Z materials, while low-Z materials interact with the same photons predominantly via Compton scattering. SNM is distinguished from other materials by inducing photofission and detecting the penetrative radiation as described above. Thus, a single system gives the flexibility of identifying isotopes and positionally locating the SNM [28].

Gamma transmission radiography has further advantages over other detection modes. One candidate reaction, ^{12}C(p,p'), has a markedly high 15.1 MeV-gamma yield when the incident proton energy approaches 20 MeV. The competing reaction channel ^{12}C(p,n) only arises with incident protons above that energy, however (See Figure 2.2.2). The lack of neutron flux in the ^{12}C(p,p') reaction provides a dose that is orders of magnitude lower than that associated with the source reaction previously discussed. Not only is reduced dose necessary for compliance with ANSI 43.14 "Radiation Safety Guidelines for Active Interrogation Systems for Security Screening of Cargo," but gamma transmission radiography also reduces the entire system footprint. Shielding requirements can dominate the system size and geometry. Also, note that the cross section for generating the 15.1 MeV gamma beam is four orders of magni-

---

[3]A monoenergetic gamma beam, however, gives a lower dose compared to the more common bremsstrahlung photon sources typically used with linear accelerators [28].

tude higher than the d-[11]B reaction. Theoretically, if the discernible count rate at the detector was held constant, a higher reaction cross section allows lower beam current, less time on station, and/or penetration through thicker shielding.
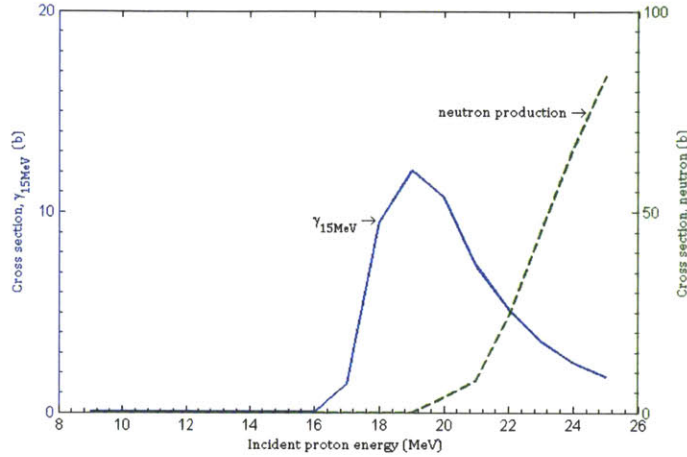
Figure 2.2.2: Cross section of the desired 15 MeV photon production from ^{12}C(p,p') and the competing ^{12}C(p,n) channel at higher energies. Data computed by TALYS [29].

Figure 2.2.3 shows a possible configuration of this type of system for the interrogation of shipping cargo. The premium on size and minimal input power is self-evident. Such a system would necessitate the accelerating gradient of a superconducting compact cyclotron.

2.2.3 Future Work

There are significant political and technical barriers to employing active interrogation for the detection of smuggled SNM. This is an area of intense research that cannot be fully review here, especially because the most relevant publications on the subject are classified. Instead, we simply point out that the next step in the development of a compact cyclotron-based system must focus on measures to increase gamma flux density at the source. This emphasis on the interrogating beam, rather than the
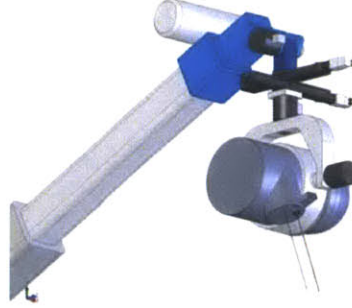
Figure 2.2.3: Possible configuration of a compact cyclotron used for active interrogation, here mounted on a typical 30-ton boom truck. The cyclotron is suspended from a telescopic boom; a secondary beam of gamma rays reacts with high-Z materials via pair production and induces photofission in actinides. These processes can be used to detect and identify actinides in cargo containers. Image used by permission of IONETIX CORPORATION.

detector, can be justified analytically.

Consider the task of passively detecting a Gaussian-like signal of SNM from a shielded cargo container. If a known background radiation yields X_B counts per second, then for one to conclude with 95% confidence that there is a signal above background, the signal intensity must exceed the à posteriori detection criteria, L_C: $L_C = 1.645\sqrt{X_B \cdot t}$, where t is the counting time. To be 95% confident that a real signal is not disregarded, the signal intensity must exceed the à priori detection limit, L_D: $L_D = 2.71 + 2 \cdot L_C$ [30].

The resolution of a detector system is usually described by the full width at half maximum $FWHM$ of the photo-peaks in its spectra. It can be shown that the lowest detection limits result if the energy window is chosen to be 1.2 times the $FWHM$, but it is common to be conservative and use a window that is twice the $FWHM$. The background X_B can be expressed as $2 \cdot FWHM \cdot b_E$, where b_E is the background count rate per keV in the region of the peak. If a detector with a front surface area of S_{det} and an intrinsic efficiency of e is exposed to a signal neutron (or photon) flux density of F in time t, it will register $F \cdot S_{det} \cdot e \cdot t$ counts. The à priori detection criteria is

$F \cdot S \cdot e \cdot t > 2.71 + 4.65\sqrt{FWHM \cdot b_E \cdot t}$. The signal flux must be greater than a critical flux density, F_C:

$$F_C = \frac{2.71}{S_{det} \cdot e \cdot t} + \frac{4.65}{S_{det} \cdot e}\sqrt{\frac{FWHM \cdot b_E}{t}}. \qquad (2.2.1)$$

The first term of Equation 2.2.1 pertains to the detection limit of the detector crystal itself. If we assume the statistics of the system are not limited by the detector but by the overwhelming background, we can ignore the first term. If we say the SNM has a flux of F_1 at 1 m, then $F_C = F_1/r^2$, where r is the critical distance in meters from the SNM that a particular detector must be in order to register the signal with 95% confidence, assuming no attenuating medium. The background flux density would be proportional to $f = b_E/S_{det} \cdot e$. Substituting these new terms into Equation 2.2.1 and solving for r gives [31]:

$$r = 0.464 \cdot \sqrt{F_1} \cdot \sqrt[4]{\frac{S_{det} \cdot e \cdot t}{FWHM \cdot f}}. \qquad (2.2.2)$$

Distance is important in active interrogation since the goal is usually to be nonintrusive or covert in the operation. From a systems perspective, greater standoff with a given detector correlates to devoting fewer resources and less risk. If the critical distance is too close for the mission set, then the detecting party must leverage more advanced technologies (cost) to improve its detection system. In this way, critical distance r is a proximate measure of effectiveness of a detection system.

Equation 2.2.2 is interesting because it contrasts the task of the detecting party with the task of the smuggler to not be detected. All parameters associated with the detector are under the fourth root: size, efficiency, collection time, resolution, and background reduction. Major efforts to improve the detector, such as designing it larger (S_{det}) or incorporating collimators for reducing background (f), result in very little increase of the stand-off distance. The smuggler's task—reduce the flux density

36

F_1 through shielding—is only under a square root [31].[4] Relatively small shielding efforts force the detecting party to engage closer in.

The strength of active interrogation is that it gives the detecting party some control over F_1 despite the smuggler's shielding. The tradeoff, however, is that the interrogating photon flux reduces by one over the distance squared on its path to the SNM, is attenuated in the shielding, then the induced radiation attenuates and disperses on its path to the detector as described above. Here we assume that the source and the detector are collocated. The 1 m neutron flux density F_1 can be expressed as a function of the interrogating photon flux density 1 m from the source, F_{γ_1}:

$$F_1 = \frac{F_{\gamma_1} \cdot t}{r^2} \cdot S_{SNM} \cdot \Sigma_{pf} \cdot \bar{\nu} \cdot e^{-(\mu_n + \mu_\gamma)}, \tag{2.2.3}$$

where S_{SNM} is the cross sectional area of the smuggled SNM, Σ_{pf} is the photofission macroscopic cross section of the SNM, $\bar{\nu}$ is the neutron multiplicity, and μ_n and μ_γ are the neutron and gamma linear attenuation coefficients associated with the 1 m thick shield environment. Rewriting Equation 2.2.3 as $r = \sqrt{F_1} \cdot D_{eff}$, and substituting Equation 2.2.2 gives the critical distance as a function of the interrogating beam density and the detection system's effectiveness (D_{eff}):

$$r = \sqrt[4]{S_{SNM} \cdot \Sigma_{pf} \cdot \bar{\nu} \cdot e^{-(\mu_n + \mu_\gamma)}} \cdot \left(\sqrt[4]{F_{\gamma_1} \cdot t} \cdot \sqrt{D_{eff}} \right). \tag{2.2.4}$$

Again the equation reflects the task of smuggler and detecting party, but now they appear more even-handed. The smuggler's decisions regarding the size (S_{SNM}), fissile purity and density (Σ_{pf}), and shielding (μ_n and μ_γ) can be directly countered with greater interrogating beam fluence ($F_{\gamma_1} \cdot t$). Future work on active interrogation with secondary gamma beams should focus on the source term. First of all, compact

---

[4]Note that the critical distance is 5-10 times larger for neutrons than for gammas. The primary difference is a lack of neutrons in background radiation. The greatest distances are due to the efficiency of ^{3}He chambers, which are no longer in widespread use. With regard to neutron radiation, it is less accurate to dismiss the first term in Equation 2.2.1.

cyclotrons need to be designed to deliver maximum ion currents. One cannot sacrifice beam current for compactness. Secondly, the gamma flux density is dependent on the choice of nuclear reaction, and more experimentation is necessary to inform those decisions. The reactions mentioned above, $^{11}B(d,n)^{12}C$ and $^{12}C(p,p')$, lack complete experimental cross sections ascertaining the energy and yield with respect to all solid angles. Additionally, there are many other reactions that should be investigated to find the largest cross section for production of gammas suitable for inducing photofission. Third, the gamma beam can be made more dense via focusing. Focusing the secondary beam requires directing the initial extracted beam to a target situated external to the cryostat of the cyclotron. These beam dynamics still require much development effort to minimize current loss.

3 Fast Neutron Imaging for Enhanced Stockpile Surveillance

Fast neutron imaging is a way of achieving high-resolution images of low-Z material behind heavy shields. The basic principle of neutron imaging is similar to that of X-ray radiography. A beam of neutrons falls on the specimen and, after passing through the specimen, leaves an image on a photographic plate or on a detector. The neutrons interact with the nuclei of the specimen's atoms, and their absorption and scattering properties make it possible to produce images of components containing light elements (like hydrogen) beneath a matrix of metallic elements (lead or bismuth), which cannot be easily done with conventional X-rays.[1] A popular demonstration of the different and complementary roles of neutron and x-ray imaging is shown in Figure 3.0.1.
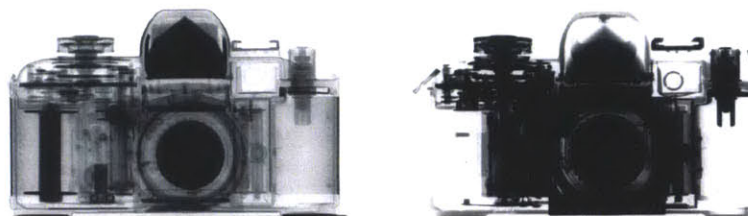

Figure 3.0.1: The image of the camera on the left was formed with thermal neutron radiography, revealing soft low-Z plastic pieces; the one on the right was formed with x-rays where the metallic components are opaque and the plastic parts are transparent.

---

[1]For a full description on the state of the art, list of facilities, and related research from around the world, see [32].

In general, fast neutrons are created in a nuclear reactor from fission or by colliding ions into a target with a particle accelerator. An imaging system's performance is largely dependent on the flux and energy spectrum of the neutron source. In the accelerator case, many factors are considered when choosing the neutron source: (1) reaction Q-value and cross section, (2) beam current, (3) target thickness and number density, and (4) ion specific energy loss. (1) and (2) are usually constrained by the accelerator available for the application, which is typically a LINAC. (3) and (4) determine the target design, and moreover, force engineering decisions about how to manage the power density from the beam. This chapter is devoted to describing and assessing alternative source-side configurations for the fast neutron imaging of the Nuclear Explosive Package (NEP) using a compact cyclotron.

3.1 Introduction

A Unique and Challenging Application

The DOE's Office of Defense Programs has the responsibility, under the Stockpile Stewardship and Management Program, of determining the safety and reliability of the U.S.'s aging nuclear stockpile. A component program called Enhanced Stockpile Surveillance (ESS) seeks to improve predictive capabilities to define age-related changes in material properties of the stockpile and to engage in preventative maintenance before a problem develops. It is very costly to disassemble the NEP to inspect certain limited-lifetime components such as neutron generators and tritium reservoirs. Imaging them in place would be a more economical and nondestructive evaluation technique for examining corrosion effects within the NEP's hermetic seal [33, 34].

A team at Lawrence Livermore National Lab (LLNL) designed one method of using fast neutrons to image these heavily shielded features (See Figure 3.1.1). A suitable source must provide monoenergetic 10 MeV neutrons at an intensity of 10^{11}

40

n/sec/sr in the forward scattered direction. The ^{2}H(d,n)^{3}He (or d-D) reaction has a favorable Q-value and cross section for generating neutrons [35]. It is known as the "work horse" of the traditional monoenergetic neutron sources [36]. The neutron spectrum from this reaction is kinematically collimated—neutron emissions are compressed into a forward cone with two neutron groups inside the cone—giving high-brightness in the forward direction, and minimal background.[2] The d-D reaction produces very little gamma radiation. The tabulated differential cross sections are very accurate, so the angular dependency of yield and energy are reliable. Other advantages are that the LINAC configuration[3] chosen to drive the deuterons exhibits reliable performance, relative compactness, low beam emittance and is commercially available.
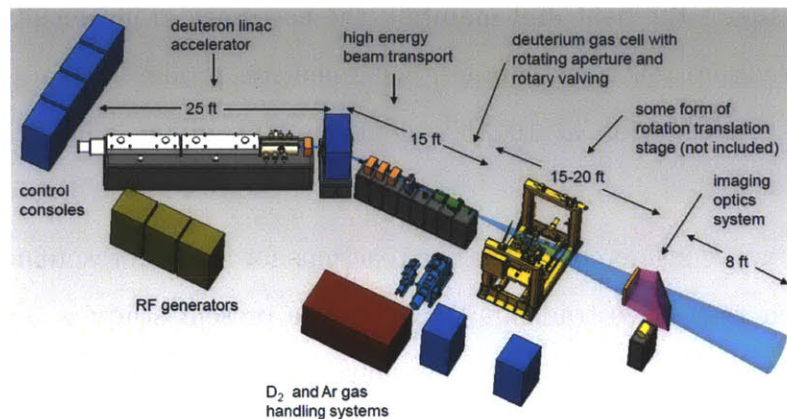
Figure 3.1.1: Proposed Enhanced Stockpile Surveillance (ESS) fast neutron imaging configuration. Schematic from [7].

There are four major complications with this method, however. First, the target design is not simple. Deuterium must be sufficiently pressurized to 3-4 atm, or 0.483 mg/cm^3, in a 4 cm chamber to achieve the required reaction rate. The beam must be stopped in an absorbent gas (e.g. Ar, Ne, or He), while not producing gammas

---

[2]Here brightness is defined as average beam intensity into 4π steradians, divided by total emission area (n/sec/cm^2). High brightness is then associated with low emissivity creating a tightly focused spot.

[3]The proposed design includes two RFQs (30 keV-2.5 MeV, 2.5-4.5 MeV) and one DTL (4.5-7.0 MeV). We will refer to this configuration henceforward in shorthand as a LINAC.

or low energy neutrons. All structural components of the gas cells must be chosen to minimize gamma contamination. Second, a pulsed accelerator is necessary to allow a compressor with a rotary-valve to pressurize the target chamber. A pulsed system with average beam power of $\sim$300 μA prescribes the LINAC-based configuration and, per Equation 1.2.3, indirectly restricts the maximum ion energy and list of candidate reactions. Third, a pulsed system with average beam power of 2.1 kW will have a peak power of 113 kW. This high brightness requires a *windowless target*. The beam intensity could rapidly deposit heat into the thin metal of a target window at a power density that would cause melt or explosion. Additionally, the beam would heat and rarefy static deuterium. The complex gas handling subsystem and pulsed beam is required to dissipate the heat and maintain the necessary atom density of the target [7]. Fourth, break-up reactions compete with neutron production, accounting for up to 25% of the cross section at 10 MeV neutrons [36], giving a *quasi-monoenergetic* spectrum.

Others have considered alternative reactions for neutron resonance imaging and have listed their respective tradeoffs [36, 32]. The present study is different because the unique aspects of the NEP prescribe neutron energies not commonly considered. Additionally, the prerequisite beam current for satisfactory image resolution is near a LINAC's functional limit. These neutron energies and beam currents are more feasibly attainable with the accelerating gradient of a cyclotron. Current product lines of compact cyclotrons suggest an alternative configuration could be implemented.

Three possibilities motivate a re-evaluation of the current technology approach for ESS. First and foremost, higher beam energies could open up different reactions with neutron-production cross sections comparable to the d-D reaction. If a solid-phase target could be found, it would greatly simplify the system design by eliminating the gas-handling subsystem, and it would ease operation and reduce overall cost and footprint. Second, if a quasi-monoenergetic spectrum is sufficient for imaging the NEP, then perhaps the competing reactions associated with solid, mid-weight targets may

42

also be permissible. Third, this application has a known feature, so the d-D reaction's stark energy variation with respect to solid angle is irrelevant. The main performance driver is neutron yield to maximize image contrast.

Problem Statement and Method of Solution

The remainder of this chapter methodically reconsiders all neutron producing reactions for ESS. Is there another reaction that may produce an image of the NEP with contrast comparable to the d-D reaction? If so, and if the required beam energy is beyond the range of a LINAC, could it be attained with a compact cyclotron? From an engineering standpoint, would that reaction be easier to implement than d-D?

Practical considerations limit our ability to fully answer these questions. First, a status quo approach for imaging the NEP using the d-D reaction is not yet developed; therefore, we will use a neutron spectrum from a windowed target to compare and evaluate the alternative reactions. Second, a suitable accelerator facility is not [yet] available at MIT to support the research and test the conclusions of this thesis. Third, given this limitation, Monte Carlo particle transport programs are utilized to simulate the thin target yields of candidate reactions. The evaluated data tables often lack essential cross sections for ion collisions, so the programs must rely on physics models. These, too, are proximate, and associated uncertainties will be discussed.

The problem is made tractable by imposing the following constraints. The detector side of the proposed imaging system is assumed ideal insofar as the prerequisite neutron flux is met. This assumption allows us to scope all possibilities that yield 10^{11} n/s/st. We limit the pool of reactions to the 56 included in the computer code DROSG-2000: NEUTRON SOURCE REACTIONS [37]. This program conveniently provides differential cross sections for every reaction, but it assumes the targets are isotopically pure. The method overlooks the possibility that there are reactions with special inelastic resonances, or compound targets that perform better. Due to a general lack of angular-dependency tabulations, we limit our search to forward scattered

yields. The benefits of kinematically collimated reactions for high neutron flux makes this a reasonable starting point. Later the angular spread of prime candidates is compared. Lastly, the maximum allowable ion beam energy is 250 MeV, which is more than enough to compare yields of even the inverse reactions in DROSG-2000 using heavy ions.

The thrust of the study is to identify exceptional neutron producing reactions, then compare the relative contrast attainable with each reaction. Section 3.2 explains the theory behind the detection of fast neutrons and signal quality, introducing and justifying the concept of relative contrast as a valid metric. Section 3.3 presents a series of tests to screen out untenable reactions for the ESS application. Section 3.4 compares the best performing reactions via simulation and qualitative analysis of potential accelerators and target design. Final results are presented in Section 3.5.

We will discover that four different reactions are potential alternatives to the d-D configuration: ^{6}Li(p,n)^{6}Be, ^{11}B(p,n)^{11}C, ^{13}C(p,n)^{13}N, and the more common ^{7}Li(p,n)^{7}Be. This last reaction could be implemented with either a LINAC or cyclotron, but the others could only realistically be implemented with a compact cyclotron. Though each has advantages and disadvantages, p-^{7}Li is the most attractive reaction for fast neutron imaging for ESS other than d-D.

3.2 Production and Detection of Fast Neutrons

Inside the NEP is a neutron generator comprising lithium deuteride (LiD) surrounded by ^{238}U tamper. Over time cracks may form in the LiD that jeopardize the reliability of the weapon to detonate as designed. While details of the specimen (the NEP) are not publishable, sub-millimeter resolution of the feature (the LiD) is required [38].

The LLNL team proposed using a plastic scintillator (BC-408) coupled with a CCD camera system for detecting the neutrons transmitted through the specimen with resonant energies. Though space does not permit a full discussion of the underlying

44

physics and tradeoffs of radiation detectors, we first review the necessary physics that determines image quality. Next, relative contrast is derived as a way to quantitatively compare the image quality of different neutron spectra.

3.2.1 Factors Affecting Signal

First, stray neutrons must be minimized. Resonant neutrons from the specimen cause proton recoils in the detector's highly hydrogenated plastic.[4] Since the interaction of neutrons with hydrogen is isotropic, the protons' recoil energy distribution is directionally independent. The recoiling proton ionizes the surrounding molecules according to the Bethe-Bloch formula, depositing most of its energy at the end of its path, which is about 100 microns. This directional displacement of the light-producing particle places a limit on the intrinsic resolution of the screen [39]. A background or elastically scattered neutron will register a signal in a position where there should *not* be a signal, degrading resolution even more. A maximum energy spread is permitted in the neutron source based on a prescribed contrast needed in the image. Neutrons with energies outside this band are noise.

Second, stray gamma rays and x-rays contaminate fast neutron radiographs and their occurrence must be minimized. The de-exciting of the ionization electrons produces visible light called fluorescence. The light interacts with amorphous-silicon (a-Si) sensor arrays on the CCD. Electron hole pairs are generated in this semiconducting material and the charge drifts under an applied electric field to a glass substrate containing anodes, which lead to the readout electronics. The chosen scintillator, BC-408, is sharply peaked at 430 nm. It is transparent to its own emission spectrum, implying that every light event will reach the CCD and be detected; however, it (and other detectors, though perhaps to a greater or lesser degree) are highly sensitive to gamma rays [40]. The beam will have competing reaction channels with the target, producing undesired gammas. This is one reason why a windowless gas target must

---

[4]H:C atom ratio in polyvinyltuolene is 1.1:1

be used in the d-D reaction configuration. Gammas interact with molecular atoms via photoelectric effect, Compton scattering, or pair production. These processes result in electrons with long erratic paths through the material ionizing molecules, producing false signals wherever they go. The light output for gammas is higher than that for neutrons, for equal amounts of energy deposited in the scintillator [39].

Third, neutron flux of the right energy is essential. Fewer than 2% of the neutrons interacting with the scintillating screen produce light [39]. The carbon atoms in the scintillator interfere and compete with the n-H interactions. Thick targets will create the most neutrons. Target thickness, however, competes with the first goal of reducing stray neutrons: neutrons produced after a few elastic collisions or ionizations have lower energy and reduce image resolution. Thin targets must be used to create neutrons within a permissible energy variation.

Fourth, angular dependence of yield and spectrum should be minimal. The angular distribution of the neutron flux and the angular dependence of the neutron energy should be sufficiently flat at forward angles to enable homogeneous exposure of large detector screens [41]. If the specimen subtends an area larger than the homogeneous spectral and flux region, then the edges of the specimen will be outside the resonance of interest. If the spectrum is forward focused, as with d-D, then the detector cannot be placed too far from the specimen, for risk of collecting stray particles. Thus the angular dependence of the neutron yield and spectrum effectively sets a limit on the size of the detector that may be used [39].

3.2.2 Signal Formulation

The statistical significance of the difference between the signal associated with the feature and the signal associated with the entire specimen is the fundamental factor for any imaging technique. Without knowing the details of the specimen or feature geometry, we may formulate a definition of contrast that will aid in the comparison of different reactions.

46

The number of neutrons interacting with any material across a linear distance x is described by

$$I(x) = I_o \, e^{-\Sigma x}, \tag{3.2.1}$$

where Σ is the total macroscopic cross section (the product of the microscopic cross section and the material number density), and I_o is the initial unattenuated neutron current. The number of neutrons reaching a detector screen after interacting with the specimen is

$$I_s = \Phi_n \, t \, A \, e^{-\Sigma_s x_s}, \tag{3.2.2}$$

where Φ_n is the uncollided neutron flux, t is time, and A is the area of the specimen at the detector screen. The number of neutrons detected after interacting with the specimen *and* the feature is

$$I_f = \Phi_n \, t \, A \, \left(e^{-\Sigma_s x_s} \right) \, \left(e^{-\left(\Sigma_f - \Sigma_s \right) x_f} \right). \tag{3.2.3}$$

Contrast is defined as the difference between the number of counts from the specimen and the counts from the feature. The *relative contrast* C is then [39]:

$$C = \frac{I_s - I_f}{I_s} = 1 - e^{\left(\Sigma_s - \Sigma_f \right) x_f}. \tag{3.2.4}$$

From this relationship we see that the contrast is maximized when the difference between the total macroscopic cross sections of the specimen and feature $(\Sigma_s - \Sigma_f)$ is minimized. In the ESS application, the LiD feature is encased within the NEP specimen. By assuming that the number density of LiD is small compared to the ^{238}U, we may approximate that the specimen refers only to the uranium. High transmission through the ^{238}U (minimum Σ_s) coupled with high absorption in the LiD (maximum Σ_f) gives the best image. The only geometry-dependent factor in the formula is the length of the feature. From the problem statement, ESS must resolve submillimeter aberrations in the LiD. Setting x_f equal to 1 mm gives a usable approximation of

relative contrast as a function of neutron energy, as graphed in Figure 3.2.1. Note that negative values imply that the specimen is more opaque to neutrons than the feature; otherwise units are arbitrary.
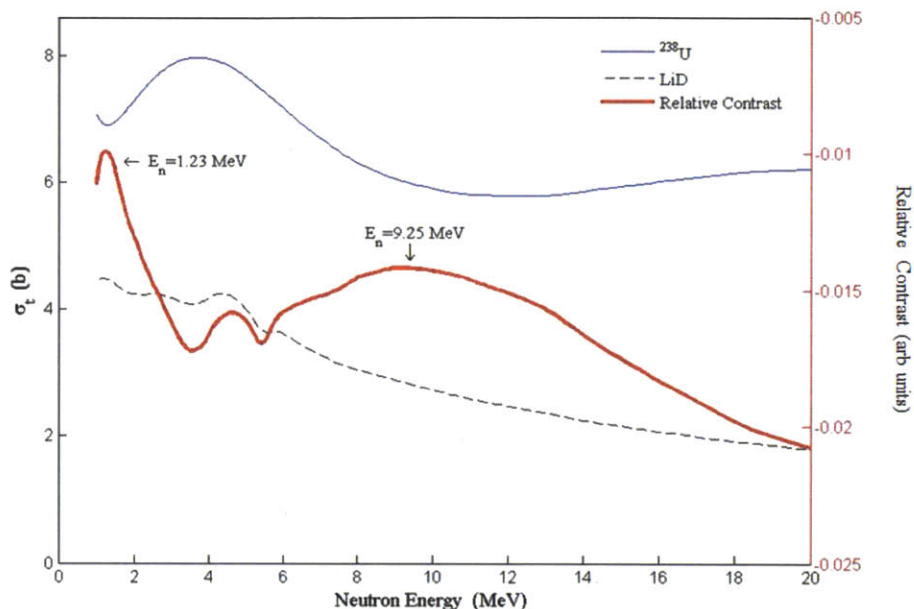
Figure 3.2.1: Total cross section of U-238 and LiD. The relative contrast is shown by the red line and read to the right. Two different peaks denote primary transmission "windows."

Regions where the relative contrast is amenable to fast neutron imaging are referred to as "transmission windows."[5] The LLNL project team focused on a transmission window extending from 6 to 11 MeV. Monte Carlo simulations found that neutrons with energy outside this band blur the image [42]. This result agrees with the analytical approach of relative contrast described above. There is a clear peak centered on 9.25 MeV in Figure 3.2.1, and the contrast curve decreases significantly at energies less than 6 and greater than 11.

The relative contrast formulation is advantageous for two reasons. First, it en-

---

[5]The terms "transmission window" and "region of interest" (ROI) are used interchangeably in this thesis.

abled the discovery of another, in fact higher, peak centered on 1.23 MeV (The LLNL team may have overlooked this transmission window). We will investigate viable reactions in both regions of interest (ROI) in this study. Secondly, since relative contrast is a continuous function existing wherever there is cross section data for the specimen and feature, it enables all incident neutrons to contribute to the image. Neutrons with energies in the ROIs contribute positively; those outside the ROI contribute negatively.

In order to compare the image quality of two different neutron spectra we use relative contrast as a multiplicative operator. To perform the operation we must translate the curve so that the relative contrast in the ROIs is positive. Relying on the observations from LLNL's simulations that neutron energies below 6 MeV are ineffective, we employ the simple transformation,

$$C'(E_n) = C(E_n) - C(E_n = 6).$$ (3.2.5)

The unattenuated neutron intensity of each energy bin multiplied by the bin's corresponding relative contrast gives a value for that bin's contribution to the image. Summing these values across the whole spectrum gives a numerical value that represents how well that spectrum, and hence the source reaction, may form an image of the NEP. We will call this value *Total Relative Contrast* (TRC). TRC has no physical meaning, but may be compared relative to other reactions, namely d-D:

$$TRC = \sum_n C'(E_n) \cdot I_o(E_n).$$ (3.2.6)

The contrast is in effect the signal. Since both I_f and I_s obey Poisson counting statistics, the standard deviation of the signal—the noise—is $\sqrt{I_s + I_f}$. Therefore the *signal-to-noise* ratio may be written,

$$\frac{S}{N} = \frac{I_s - I_f}{\sqrt{I_s + I_f}} = C\sqrt{\frac{I_s}{2 - C}}.$$ (3.2.7)

The signal-to-noise relationship is the preferred way to compare imaging techniques. Equation 3.2.7 shows that the signal can double in two ways: (1) the contrast must double, by increasing the feature size (x_f) and/or selecting reaction kinematics that exploit optimum transmission windows; or (2) the neutron flux (Φ_n) or acquisition time (t) must increase by a factor of four. Unfortunately, the signal-to-noise equation requires knowledge of the specimen geometry to inform total counts from the specimen. Without access to that information about the NEP, we settle for the imperfect yet sufficiently accurate relative contrast formula to compare signal qualities of different reactions.

In summary, nuclear reaction criteria for fast neutron imaging applied to ESS include:

- Maximize neutron production; no less than 10^{11} n/s/sr.

- Limit neutron energy spread; less than 1 MeV, centered on 9.25 MeV or 1.23 MeV.

- Minimize stray neutrons; energies outside the 6-11 MeV or 1-2 MeV transmission windows contribute negatively to the image.

- Minimize gamma radiation.

- Minimize angular dependence of neutron energy and intensity.

3.3 Initial Screening

This section explains how viable reactions are identified through inspection of acceptability, inherent energetics, stopping power, and cross sections.

3.3.1 Acceptable Reactions

We begin by including all 56 neutron-producing reactions from DROSG-2000 in the study. The targets are assumed to be isotopically pure, residing in the state (solid, liquid, or gas) in which they exist under normal laboratory conditions. This simplifying assumption aims to maximize reaction rate and minimize contaminating radiation from other elements in molecular compounds.

Reactions may be automatically rejected for three reasons. First and foremost, in an effort to simplify the system design and optimally exploit the CW beam, we eliminate all gas-phased targets. Second, radioactive targets or projectile ions (^{3}H) are disregarded. Third, targets that emit hazardous vapors (Be) are unacceptable in most operational settings under the DOE Chronic Beryllium Disease Prevention Program.[6] The short list of reactions that survive this initial cut are listed with their Q-values in Table 3.1.[7]

Table 3.1: List of candidate neutron-producing reactions utilizing solid, nonhazardous targets. The gaseous d-D reaction is listed as the standard for comparison. Reaction Q-value, in MeV, is shown in parentheses.

^{2}H(d,n)^{3}He (3.27)	^{11}B(p,n)^{11}C (-2.76)	^{36}Cl(p,n)^{36}Ar (-0.07)	^{13}C(d,n)^{14}N (5.33)
^{7}Li(p,n)^{7}Be (-1.64)	^{12}C(p,n)^{12}N (-18.1)	^{59}Co(p,n)^{59}Ni (-1.86)	^{24}Mg(d,n)^{25}Al (0.05)
^{6}Li(p,n)^{6}Be (-5.07)	^{13}C(p,n)^{13}N (-3.00)	^{7}Li(d,n)^{8}Be (15.031)	^{28}Si(d,n)^{29}P (0.52)
^{10}B(p,n)^{10}C (-4.43)	^{14}C(p,n)^{14}N (-0.63)	^{11}B(d,n)^{12}C (13.7)	^{32}S(d,n)^{33}Cl (0.05)

3.3.2 Energetics

The projectile must provide enough energy to compensate for negative Q-values and overcome threshold energies. The reaction Q-value is the difference between the rest mass energies of the initial and final states of all nuclei involved in the reaction. Positive

---

[6]See 10 CFR Parts 850, Final Rule (2006); and the implementation guidance in DOE G 440.1-7A; both available at www.hss.doe.gov/healthsafety/wshp/be/.

[7]Q-values were obtained from [43], which utilizes the 2003 Atomic Mass Evaluation (G. Audi, CSNSM Orsay, France).

Q-value means a more stable product nucleus is achieved. The difference in binding energy is transferred to any ejected particles, less any energy retained to place the product nucleus in an excited state. A negative Q-value means energy is consumed to achieve the desired product. This energy must come from the kinetic energy of the projectile. Once the reaction Q-value is exceeded, the energy of the ejected neutron E_n increases with beam energy E_b according to:

$$E_n - Q = \frac{4\ (A_{tgt}/A_b)}{(1 + A_{tgt}/A_b)^2} \left(\cos^2 \theta\right) E_b, \qquad (3.3.1)$$

where A_{tgt} and A_b are the mass of the target and beam particles respectively, and θ is the neutron scattering angle in the laboratory reference frame [44]. This equation assumes all kinetic energy is transferred to the neutron, neglecting the kinetic energy of the recoiling nucleus. The program CATKIN 2.02 was useful for determining the precise ejected neutron energy from single beam energies [45]. Though neutron energy is highest in the forward direction, we are interested in the whole range of possible beams. A MATLAB script was developed to automate the calculation.

Allowing $E_n \in [1, 2] \cup [6, 11]$, a matrix of all possible beam energies and scattering angles for each reaction was computed. Only ground state products were considered for now. Heavier targets may have resonances in their cross sections stemming from complicated excitation functions which could yield monoenergetic neutrons. Some prominent examples are ^{15}N(p,n)^{15}O [46], ^{25}Sc(p,n)^{45}Ti [47], and ^{51}V(p,n)^{51}Cr [48]. These heavier elements, however, have lower center-of-mass momentum, and only produce neutrons in the keV range.

The DROSG-2000 program was used to determine differential cross sections from this matrix of beam energies and ejectile angles. With the exception of a few reactions that the program's author measured, DROSG-2000 draws all cross section data from the ENDF libraries [37]. As already stated, these results may be based on scant experimental data or be otherwise flawed. For many reactions of interest, an

isotropic approximation from integrated cross sections is used (i.e. the differential cross section in the specified steradian is determined by the total cross section divided by 4π). In general, the neutron emission is forward-peaked, and the neutron intensity over the solid angle subtended by the sample or detector is optimal in the forward direction. Thus, we reduce the field of possibilities for each energetically viable reaction to evenly spaced beam energies corresponding to 8-11 MeV, or 1-2.5 MeV, neutrons ejected at the 0° angle. These data are presented in Table 3.2.

3.3.3 Target Design

Production of monoenergetic neutrons is critically dependent on the target thickness. According to Equation 3.2.1, the neutron flux produced is proportional to the ion current striking the scattering or absorbing material and on the thickness of the material. The probability that a particle will interact with the target within a distance t, e.g. the target thickness, is given by,

$$F(t) = \int_o^t \Sigma \, e^{-\Sigma x} \, dx = 1 - e^{-\Sigma t},$$ (3.3.2)

and,

$$\Sigma = N \left(\sigma_{scatter} + \sigma_n + \sigma_{rad.\,capture} ... \right).$$ (3.3.3)

Thus, the probability of a neutron-producing collision increases with target thickness, but so does unwanted scatter. Since the cross section for scatter is almost always greater than neutron production, thick targets will moderate the projectiles with elastic or inelastic collisions before the ion is absorbed by a nucleus to eject a neutron. The neutron will take on the kinetic energy of whatever is left over after the scatters and Q-value. This stochastic energy loss is called energy straggling and results in an emission spectrum that is unusable for fast neutron imaging. If the target is too thin, neutron flux will be unnecessarily small.

Table 3.2: Optimum beam energies for energetically-viable neutron-producing reactions. Differential cross sections are shown that correspond to discrete beam energies. Fewer points are necessary to characterize reactions compatible with the 1-2 MeV region since it is a smaller transmission window.

Neutron Energy Range	Energetically Viable Reactions	Beam Energies (MeV)					Differential Cross Section (mb/sr)				
		1	2	3	4	5	1	2	3	4	5
6-11 MeV	2H(d,n)3He	2.80	4.40	6.01	7.00	7.70	52.63	68.93	81.23	87.53	90.97
	7Li(p,n)7Be	7.70	9.75	10.87	11.58	12.60	11.71	5.25	3.82	3.74	3.90
	6Li(p,n)6Be	11.20	13.25	14.38	15.08	16.00	12.42	13.84	14.47	no data	no data
	10B(p,n)10C	10.50	12.50	13.69	14.33	15.40	0.38	0.42	0.37	0.34	0.33
	11B(p,n)11C	8.80	11.00	12.00	12.67	13.70	15.84	26.97	20.43	16.57	10.99
	12C(p,n)12N	24.70	26.24	27.77	28.59	29.40	0.32	0.38	0.38	0.39	0.39
	13C(p,n)13N	9.10	11.25	12.24	12.92	13.90	10.49	15.30	11.48	9.69	6.26
	14C(p,n)14N	6.70	8.75	9.85	10.58	11.50	3.43	4.01	2.96	3.33	2.21
	59Co(p,n)59Ni	7.90	10.00	11.10	11.83	12.80	11.71	18.32	22.34	25.59	29.19
	13C(d,n)14N	1.00	2.75	3.93	4.58	5.60	1.82	2.51	2.65	2.57	2.41
	24Mg(d,n)25Al	6.00	8.00	9.25	9.33	11.00	1.1E-03	1.1E-03	1.1E-03	1.1E-03	1.1E-03
	28Si(d,n)29P	5.50	7.75	8.75	9.25	10.50	5.3E-02	5.3E-02	5.3E-02	5.3E-02	5.3E-02
	32S(d,n)33Cl	6.00	8.00	9.23	9.33	10.90	5.5E-02	5.5E-02	5.5E-02	5.5E-02	5.5E-02
1-2 MeV	7Li(p,n)7Be	2.80	3.60				53.54	41.18			
	6Li(p,n)6Be	6.50	7.30				2.72	5.31			
	10B(p,n)10C	5.70	6.50				0.07	0.15			
	11B(p,n)11C	3.90	4.80				6.39	12.31			
	12C(p,n)12N	20.20	20.90				0.01	0.06			
	13C(p,n)13N	4.10	5.00				5.53	9.26			
	14C(p,n)14N	1.70	2.60				1.13	2.45			
	59Co(p,n)59Ni	2.90	3.80				0.93	2.34			
	24Mg(d,n)25Al	1.00	1.90				1.1E-03	1.1E-03			
	28Si(d,n)29P	1.00	1.40				5.2E-02	5.2E-02			
	32S(d,n)33Cl	1.00	1.90				5.4E-02	5.4E-02			

Figure 3.3.1 shows an MCNP tally of neutron intensity from the ^{7}Li(p,n)^{7}Be reaction, where the lithium target thickness varies from 0.10 mm to 5 mm. The neutron yield is greatest with the thick 5 mm target, but the energy spectrum is diffuse. The thinnest target in this example has the sharpest peak—highest kurtosis—but the flux of neutrons is one third that of the 0.32 mm target. Note that for thin targets the mean neutron energy decreases by a factor proportional to the peak width.
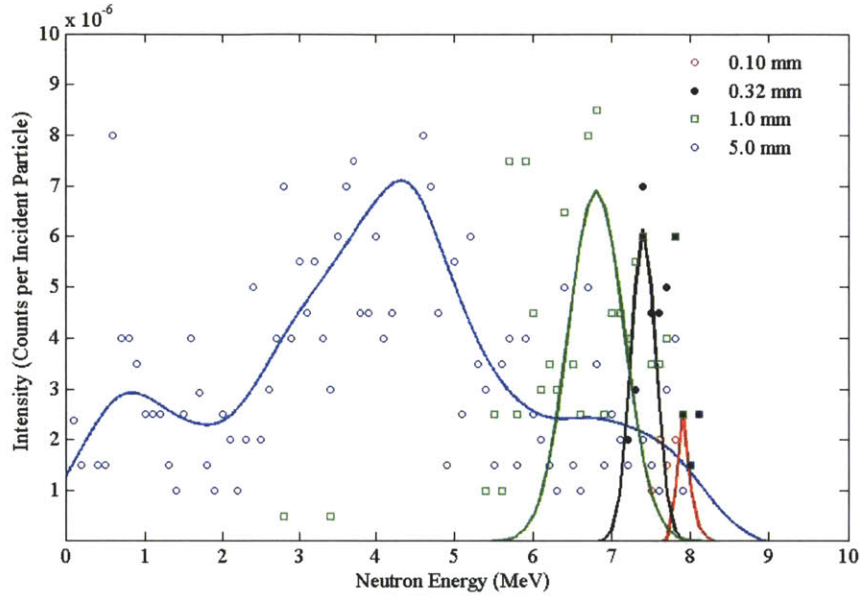
Figure 3.3.1: Neutron spectrum from ^{7}Li(p,n)^{7}Be simulation in MCNPX [49]. The proton beam was modeled as a 9.75 MeV point source; results are tallied from a surface subtending one steradian off of beam line; error bars are omitted for clarity; solid lines are fitted curves intended to guide the eye. The solid black line represents the maximum target thickness allowed for a 600 keV energy spread. Energy straggling in thicker targets is obvious, while the thinner 0.10 mm target yields fewer neutrons.

The goal then is to find a target thickness that maximizes neutron yield while limiting the energy spread to what is acceptable for the resonance structure of the feature and for empirical performance of the imaging instrumentation. The feature and detection instrumentation chosen by LLNL permit an energy spread less than or equal to 1 MeV [50].

The differential energy loss $-dE/dx$, or linear stopping power $S(E)$, of charged particles in an absorber is explicitly given by the Bethe formula:

$$S(E) = -\frac{dE}{dx} = \frac{4\pi e^4 z^2}{m_o v^2} N Z \left[\ln \left(\frac{2 m_o v^2}{I} \right) - \ln \left(1 - \frac{v^2}{c^2} \right) - \frac{v^2}{c^2} \right], \qquad (3.3.4)$$

where ze and v are the charge and velocity of the primary particle, m_o is the electron rest mass, c is the speed of light, and N and Z are the number density and atomic number of the absorber [51]. The parameter I is the average excitation and ionization potential of the absorber. It can be found in tables, or approximated for elements with $Z > 12$ [52]:

$$I \, (\text{eV}) = \left(9.76 + 58.8 \, Z^{-1.19} \right) \cdot Z. \qquad (3.3.5)$$

The maximum target thickness may be estimated:

$$t = \int_{E_o}^{E_1} \frac{dx}{dE} \, dE = \frac{1.0 \, (\text{MeV})}{S(E) \, (\text{MeV}/\text{mm})}. \qquad (3.3.6)$$

3.3.4 Characterization of the Source

The total neutron yield Y_n is the convolution of the stopping power and the cross section, both functions of beam energy:

$$Y_n = \Phi_{ion} \, N \int_{E_o}^{E_1} \frac{dx}{dE} \, \sigma_n(E) \, dE, \qquad (3.3.7)$$

where Φ_{ion} is the beam current (ions/sec), $\sigma_n(E)$ is the differential microscopic cross section for neutron production (mb/sr), and N is the target number density (atoms/cm^3).

We may estimate the beam current required to achieve a yield of 10^{11} n/s/sr by solving Equation 3.3.7 for Φ_{ion}. Curves are presented in Figure 3.3.2 and Figure 3.3.3 for the 6-11 MeV transmission window and for the 1-2 MeV transmission window respectively. The curves are truncated to bring attention only to the beam energies

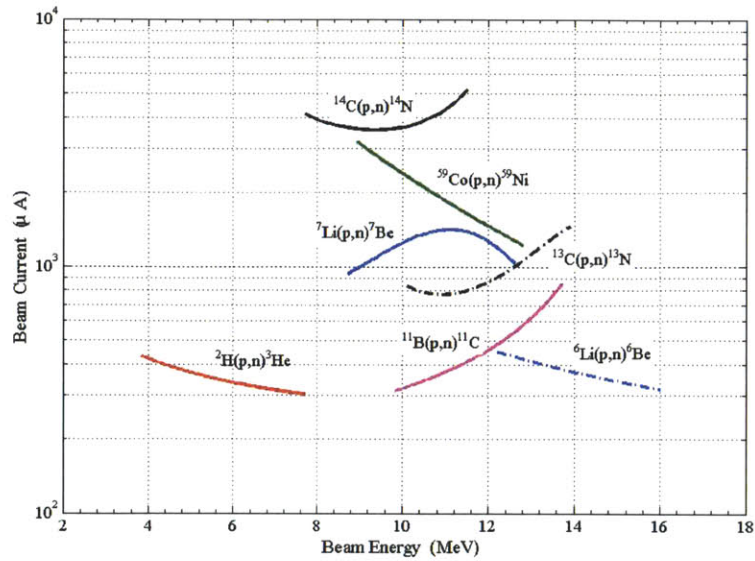that pair with suitable neutron energies.

Figure 3.3.2: Required current to yield 10^{11} 6-11 MeV neutrons per second per steradian, allowing a 1 MeV neutron energy spread.
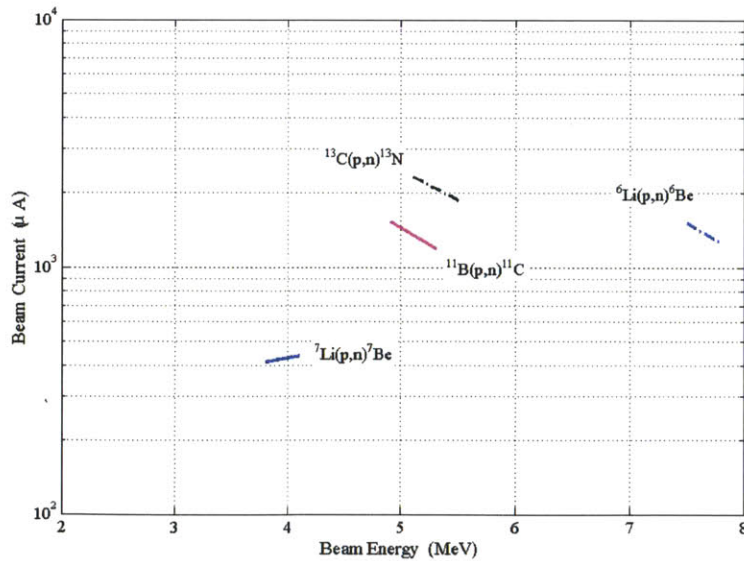

Figure 3.3.3: Required current to yield 10^{11} 1-2 MeV neutrons per second per steradian. Other reactions requiring higher than 10 mA of beam current are ignored.

Figure 3.2.1 indicates that different neutron energies within each transmission window produce different image qualities due to the absorption spectrum of the specimen. Selecting a beam energy that optimizes neutron yield may inadvertently select neutron energies near the edge of the transmission window with poor contrast. Required current and relative contrast may be related through Equation 3.2.4 and Equation 3.3.1. Figure 3.3.4 displays the relationship graphically for the five reactions, including d-D, that are energetically viable under 1 mA of particle beam. Though the numerical difference in relative contrast is small—a thousandth of a percent—the difference in performance of 6 MeV versus 9.5 MeV (-0.0151% vs -0.0141%, respectively) is significant. The tradeoff in current and contrast for the d-D and p-^{6}Li reactions is not severe. The tradeoff for p-^{11}B and p-^{13}C is more noteworthy.
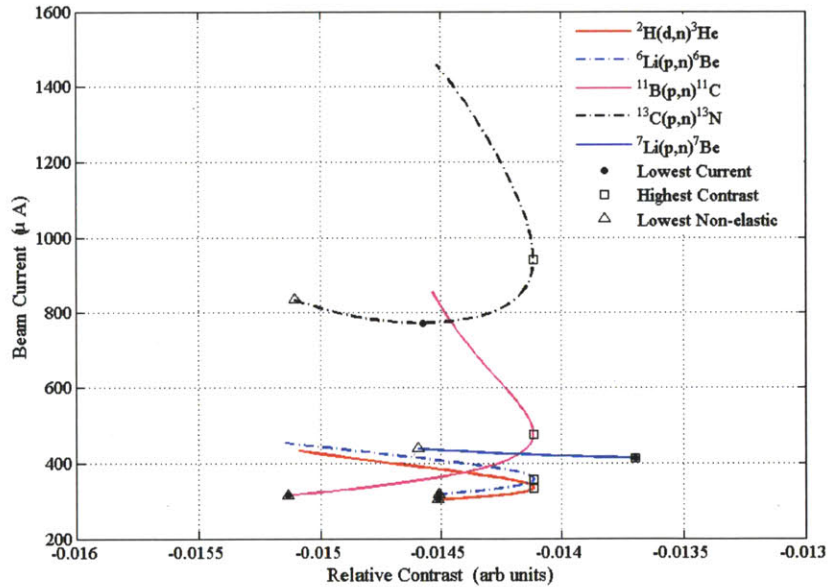
Figure 3.3.4: Relative contrast versus required beam current. With the exception of ^{7}Li(p,n)^{7}Be yielding 1-2 MeV neutrons, each reaction demands a tradeoff between current and image quality. For instance, the lowest possible beam current to yield 10^{11} neutrons via the ^{11}B(p,n)^{11}C reaction is comparable to the d-D reaction's current (~300 μA); however, to achieve comparable image contrast with 9.25 MeV neutrons, the proton current must increase about 200 μA.

Figure 3.3.4 also identifies the required current and relative contrast at the beam energy where non-elastic scattering is minimized. Non-elastic scattering includes inelastic scattering plus all other competing reaction channels. Break-up reactions—when the target nucleus breaks into three or more constituent parts—is especially pertinent at these energies for light targets [53]. Non-elastic scattering will influence both the image quality and neutron yield by broadening the neutron spectrum. Ions lose energy to the excitation of the target nucleus. Figure 3.3.5 shows the inelastic scattering cross sections of the five selected reactions, again emphasizing the energy bands that correspond with transmission windows.
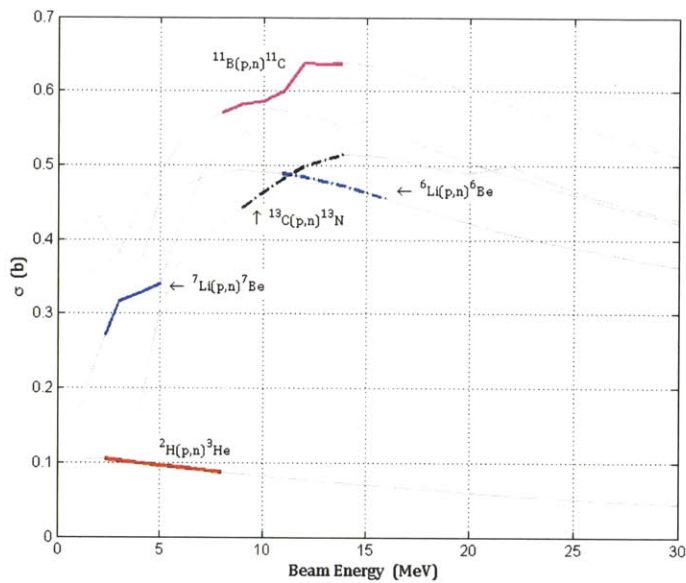
Figure 3.3.5: Non-elastic scatter cross sections of the energetically viable reactions requiring less than 1 mA of beam. The energy range that corresponds to transmission windows is emphasized. Data retrieved from TENDL-2009, JENDL/HE-2007, and ENDF/B-VI.8 (for the d-D reaction).

Best case scenarios are identified that minimize beam current, maximize image quality, and minimize non-elastic scattering. Reactions requiring more than 1 mA of beam current are discarded, leaving only ^{6}Li(p,n)^{6}Be, ^{11}B(p,n)^{11}C, ^{13}C(p,n)^{13}N, and

^{7}Li(p,n)^{7}Be remaining for comparison. These reaction configurations are summarily presented in Table 3.3. It is interesting at this juncture to point out that the p-^{7}Li reaction in the 1-2 MeV transmission window offers markedly improved contrast over d-D with comparable beam current. The d-D reaction, however, poses the least losses to non-elastic scatter.

Table 3.3: Summary of data for solid targets that can produce sufficient flux of monoenergetic neutrons with less than 1 mA beam current. Both transmission windows are included. The table is divided for lowest current, highest contrast, and lowest non-elastic scattering in order to show the tradeoff between current, beam energy, and image quality. An optimal system may fall somewhere between these bounding limits.

Neutron Energy Range	Energetically Viable Reactions	Beam energy (MeV)	Differential cross section (mb/sr)	Scattering cross section (mb)	Target stopping power (MeV/mm)	Targt thickness (cm)	current for 10^{11} neutrons (uA)	Neutron energy (MeV)	Relative contrast %
Measured									
6-11 MeV									
	2H(d,n)3He	7.3	89.1	89.7	0.006	4.000	309.3	10.5	-0.0144
Lowest beam current									
6-11 MeV									
	6Li(p,n)6Be	16.0	15.1	455.1	1.599	0.063	317.5	10.9	-0.0145
	11B(p,n)11C	9.8	34.6	583.2	8.703	0.011	313.7	7.1	-0.0151
	13C(p,n)13N	10.9	16.0	480.5	8.068	0.012	773.0	7.9	-0.0146
1-2 MeV									
	7Li(p,n)7Be	3.8	38.1	328.6	4.516	0.022	413.7	2.1	-0.0137
Highest image contrast									
6-11 MeV									
	6Li(p,n)6Be	14.5	14.5	468.2	1.740	0.057	358.0	9.4	-0.0141
	11B(p,n)11C	12.1	19.6	626.7	7.501	0.013	476.1	9.4	-0.0141
	13C(p,n)13N	12.4	11.8	500.8	7.251	0.014	939.8	9.4	-0.0141
1-2 MeV									
	7Li(p,n)7Be	3.8	38.1	328.6	4.516	0.022	413.7	2.1	-0.0137
Lowest Non-elastic Scatter									
6-11 MeV									
	6Li(p,n)6Be	16.0	15.1	455.1	1.599	0.063	317.5	10.9	-0.0145
	11B(p,n)11C	9.8	34.6	583.2	8.703	0.011	313.7	7.1	-0.0151
	13C(p,n)13N	10.1	15.8	465.9	8.572	0.012	835.2	7.1	-0.0151
1-2 MeV									
	7Li(p,n)7Be	4.1	33.5	328.4	4.207	0.024	438.7	2.4	-0.0146

3.4 Comparison of Viable Alternatives

This section compares the ^{6}Li(p,n)^{6}Be, ^{11}B(p,n)^{11}C, ^{13}C(p,n)^{13}N, and ^{7}Li(p,n)^{7}Be reactions vis-à-vis their spectra, required cyclotron, and engineering considerations related to the target. The spectra, retrieved through Monte Carlo simulation, reasonably informs image quality for the application. The required cyclotron informs system size and feasibility. A discussion of each reaction is detailed in the following section.

3.4.1 Simulation Model and Results

This thesis used MCNPX to model the ion beam impingement on thin targets for each reaction's so-called *low current*, *high contrast*, and *minimal non-elastic* configurations [49]. Only one configuration was used for the d-D reaction so that the others could be compared against it. The ion source was designed as a monoenergetic beam with a Gaussian distribution over one square centimeter. For simplicity, the energy spread due to the beam emittance was ignored. The target was set large enough to contain the whole beam and its thickness set as described in Table 3.3—backing material and all accelerator and experimental structure is ignored in the model. Neutron and photon flux and energy is tallied on a surface subtending exactly one steradian in the forward direction, as well as on a sphere encompassing the target.

The direct signal and background consist of all neutrons and gammas which are collected one steradian in the 0° direction from beam line. Figure 3.4.1 presents these results for each reaction. The indirect signal and background consists of all neutrons and gammas that scatter in other directions. These radiations may activate other objects in the room, scatter back to the detector and degrade the signal, or otherwise damage the instrumentation. These results are presented in Figure 3.4.2.
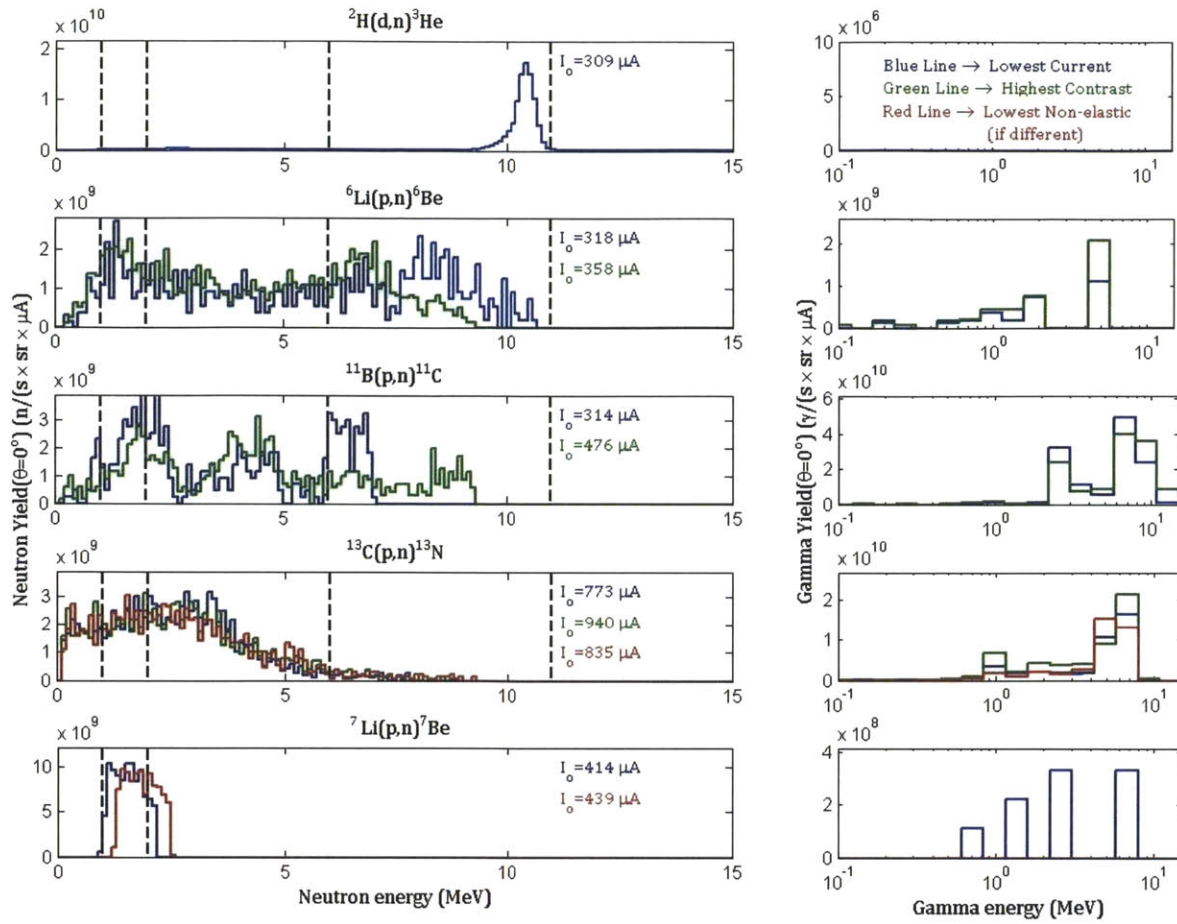
Figure 3.4.1: Yield from neutrons and gammas 0° from beam line simulated with MCNPX [49]. Error bars have been omitted for clarity. Dashed lines on left plots identify region of interest (ROI), i.e. the specimen's transmission window. Neutrons in the ROI contribute to a visible image, all other neutrons and gammas degrade the signal.
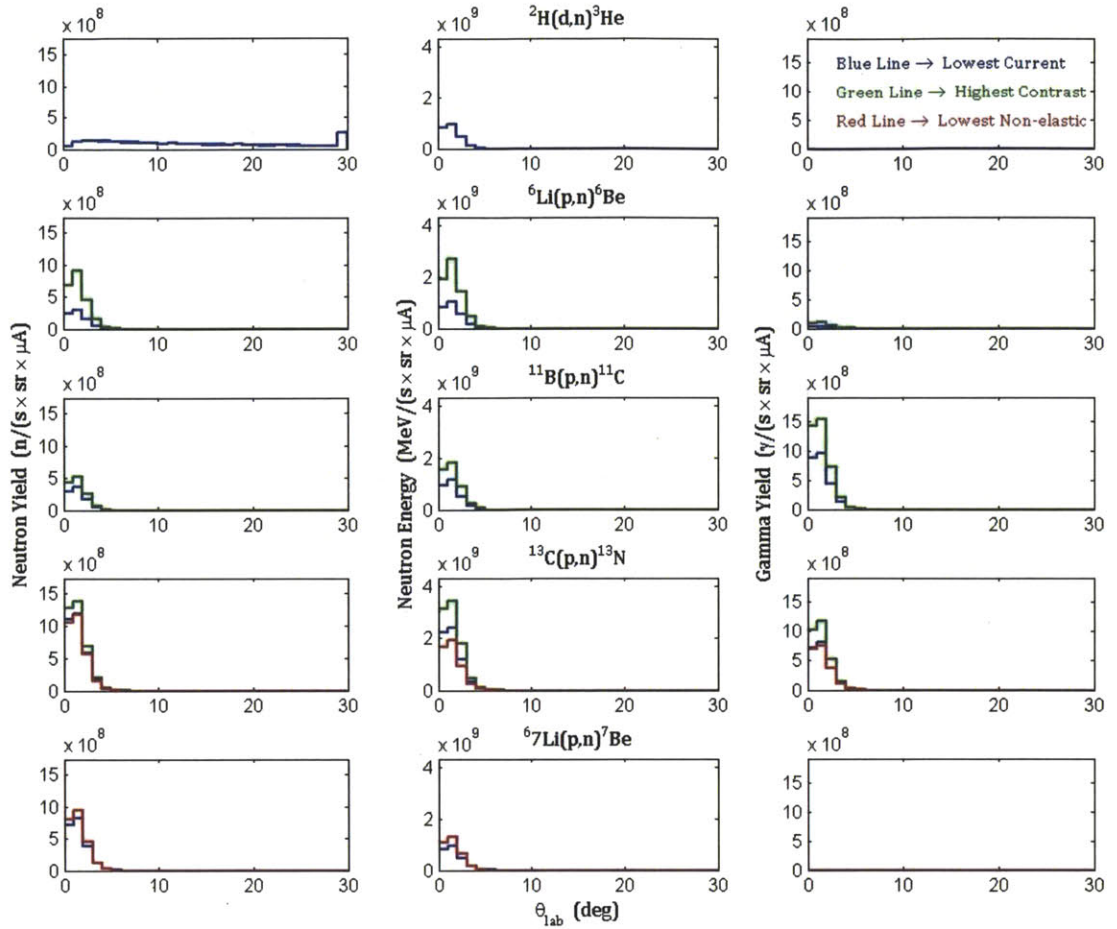
Figure 3.4.2: Indirect signal radiating from each reaction, simulated with MCNPX [49]. Plots in the left column shows neutron yield angular dependence for each reaction; the middle column shows neutron energy angular dependence; the right column shows gamma yield angular dependence. Note that the 30⁰ bin tallies all current from angles 30-180⁰.

Some initial discussion about these results is due. First, being a Monte Carlo code, the results have statistical variance, but the error bars have been omitted for clarity. The displayed results are the average of multiple independent runs, and are converged (standard deviation < 5%) with the exception of yield and energy tallies at 4⁰ angles and above. These exceptions cannot be treated as at all accurate. The direct gamma background is accurate to within a factor of two.

Second, though the variance implies convergence, the results must be read in

view of an epistemological hurdle in this analysis. Evaluated nuclear data files (ENDF) do not exist for differential cross sections of proton beams on any of these isotopes at these energies. The MCNP code cannot sample from a distribution of cross sections and excitation functions. Lacking complete libraries, the code relies on physics models[8] that are not experimentally benchmarked. Moreover, these models do not prescribe angular variation aside from the two-body kinematical relationship in Equation 3.3.1, which does not account for quantum mechanical phenomena [54]. The most glaring indicator of the model's inaccuracy is the wide disparity between actual and predicted yields. Correction was made by normalizing the per-incident-particle tally to the analytically estimated beam current of Table 3.3.

If the ENDFs were complete, and MCNPX interpolated those tables, the neutron histograms in Figure 3.4.1 would be smoother with more identifiable spectral structure in 10 keV bins, and there would be a smooth distribution across all solid angles in Figure 3.4.2 as there is for the d-D reaction. Despite this shortcoming, the direct and background yields may be considered proximate for two reasons. There is correlation between the gamma spectra and excitation functions described in nuclear literature. The angular distributions reflect the tight, kinematically-collimated cone of scatter characteristic of double-valued reactions.

Third and most pertinent to the ensuing analysis, we immediately see that p-^{6}Li, p-^{11}B, and p-^{13}C reactions bear no semblance of "monoenergetic" spectra. The spectrum flattening seen on the left in Figure 3.4.1 is not predicted by the energy straggling of Equation 3.3.4 but, rather, is predominantly influenced by the ejected neutron losing energy to the excitation of the recoil nucleus. The peaks on the right of Figure 3.4.1 correspond to de-excitations from those higher energy states.

We see that inelastic scattering dominates in these (p,n) reactions with midweight elements. The energy threshold for break-up reactions also flattens the spectra.

---

[8]MCNPX uses the Bertini model to simulate low-energy intra-nuclear cascades, and the Dresner evaporation model to simulate the de-excitation of the secondary charged particle [54].

The effect is so severe that the terms *lowest current* or *highest contrast* effectively carry no meaning except to provide useful bounding parameters. Identifying optimal contrast and yield configurations is an iterative and empirical process. A suitable experimental facility is regrettably unavailable for development of this thesis, so conclusions must be drawn from simulated results. Some iterative simulation runs were performed, but those results are not presented because the ROI neutron yields did not improve or only improved marginally.

3.4.2 Evaluating the Spectra

This section evaluates the spectra observed in Figure 3.4.1. Attempts are made to improve the neutron spectra by addressing the complications of each reaction's unique excitation functions and competing reaction channels. In general, this analysis involves looking at the spatial distribution of inelastically scattered ions to identify what target thickness prohibits their subsequent interaction.

^{2}H(d,n)^{3}He This exceptional spectrum explains why d-D is the reaction of choice for neutron imagers. The presence of an insignificent flux of low energy neutrons resulting from the break-up of deuterium is barely perceptible in the plot. This flux causes noticeable but minor range straggle in the peak. The yield is quite monoenergetic, exhibiting nearly the prescribed energy spread of 1 MeV. 95% of the neutrons reside in the ROI. Simple adjustment of beam energy, or incidence angle, will translate the peak to the optimum neutron energy of 9.25 MeV.

^{6}Li(p,n)^{6}Be ^{6}Li yields the highest flux of 6-11 MeV neutrons as expected under the *lowest current* configuration: a beam energy of 16 MeV, target thickness of 0.063 cm, and beam current of 318 μA. Incidentally, this configuration also results in the best total relative contrast as computed by Equation 3.2.6. 46% of the neutron spectrum resides in the 6-11 MeV ROI, which is bested only by the ^{7}Li spectra, but this result is still unsatisfactory compared to the d-D reaction.

66

The spectrum has two very obvious peaks and a continuum. These features are explained by the excitation functions of the target and recoil nucleus. ^{6}Be has a low-level state at 1.67±0.05 MeV, with a width of 95±28 keV [55]. The resolution of the spectrum would at best be ~2 MeV were scattering not considered. The leftward shift from the expected neutron energy (10.9 MeV for the blue peak and 9.4 MeV for the green peak) is due to inelastic scattering in the target. ^{6}Li has four energy levels below the beam energy, two of which (2.19 and 5.37 MeV) show up prominently in the gamma spectrum [56]. A neutron continuum forms as a result of this phenomenon and of multiple scatters, amassing neutrons in a low energy peak. This reaction also competes with ^{6}Li(p,pn)^{5}Li [57].

Inelastic scattering is inevitable, but its impact on the neutron spectrum can be lessened by reducing the target thickness to where the ejected proton will be unlikely to interact. The program SRIM can be used to identify the path length of the scattered protons. Setting the target thickness below the path length of the least energetic proton (corresponding to the highest possible, and probable, target excited state) is the only way to achieve a monoenergetic spectrum.

The new target thickness would have to be approximately 40 μm for the 16 MeV beam configuration, as depicted in Figure 3.4.3 below. By Equation 3.3.7, the required beam current to achieve 10^{11} n/s/sr is 5 mA.
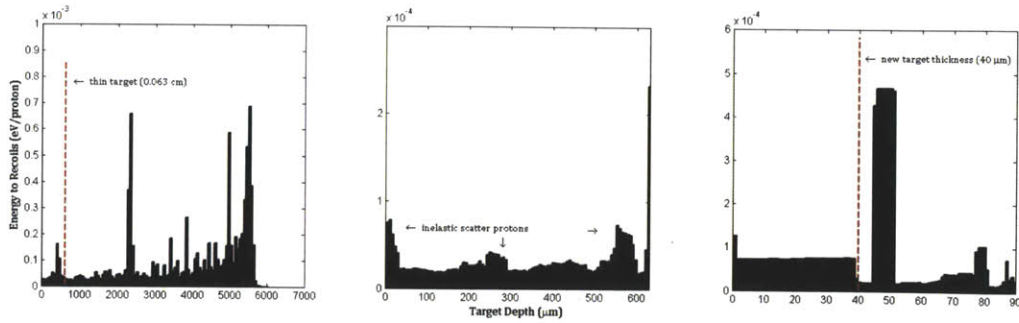
Figure 3.4.3: The full Bragg curve for p-^{6}Li (16 MeV) is shown on the left, identifying the target thickness from Equation 3.3.6. The middle plot shows the prominent points of energy deposition due to inelastically scattered protons. Designation of a new target thickness to prevent interaction of scattered protons is shown on the right. Plots generated by SRIM.

Figure 3.4.4 presents the approximate spectrum from Monte Carlo simulation. The same caveats apply with regard to the limitations of the physics models. One sees a peak begin to form near 6 MeV. Iteratively adjusting the beam energy and target thickness according to the stopping power will shift the peak near the center of the ROI, however, the low energy neutrons remain from elastic scattering. The system will be statistically-limited due to the low chance of interaction in such a thin target.

Figure 3.4.4: Simulated neutron spectrum from 16 MeV protons on 40 μm ^{6}Li. Simulation limitations prevent good resolution; a peak emerges near 6 MeV.

68

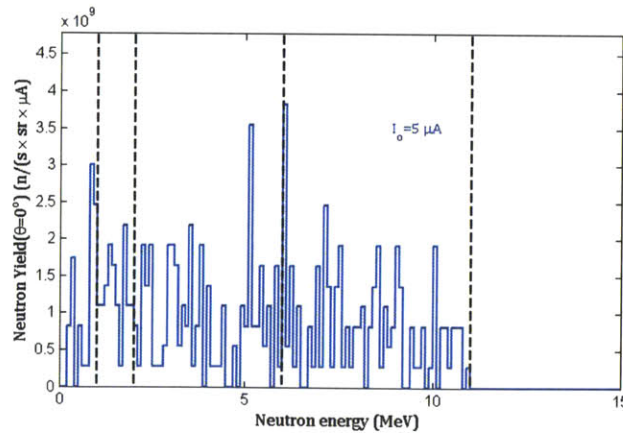**^{11}B(p,n)^{11}C** ^{11}B yielded the most neutrons in the 6-11 MeV ROI with the *highest relative contrast* configuration: 476 μA of 12.1 MeV protons on a 0.013 cm thick target. A division between three distinct peaks landed only 27% of the spectrum in the ROI.

^{11}B has thirteen unique energy levels below 12 MeV available to the (p,p') reaction, and these are known to be insensitive to input energy [58]. Some of these levels are close together so that they may be grouped ±500 keV. Doing so reduces the list to seven, three of which are prominent in the gamma spectrum: 2.12±0.03, 6.77±1.8, and 7.55±0.8, which explains the three or more peaks with a width of about 1-2 MeV. The ^{11}C target has an equal array of excited states. Though examining a slightly different energy range, one study showed eleven distinct neutron groups from a 22 MeV proton beam [59]. There were no other references found that discuss neutron thresholds.

Unlike ^{6}Li, ^{11}B's non-elastic cross section decreases with lower energy. For this reason it was considered worthwhile to follow the method described above to see if a peak could be resolved with a thinner target at a lower energy. It was found that the target would have to be 7.5 μm to avoid the first group of inelastically scattered protons; equating to a beam current of 8.25 mA.

^{13}C(p,n)^{13}N ^{13}C yielded the most neutrons in the ROI with the configuration for the lowest nonelastic scatter: 835 μA of 10.1 MeV protons on a 0.012 cm target. The spectrum is incompatible with fast neutron imaging since only 5% of the total yield was in the designated ROI. The energy-level diagram of ^{13}C is dense with lines in the energy regime of the tested protons. The target nucleus's strong affinity for energetic protons is evidenced by the tendency of the ion to deposit its energy early in its path through the target. Rickards, et al report that the only populated level of ^{13}N above ground state is 3.25 MeV with a width of 40 keV [60]. One surmises then that the lack of any peak whatsoever is due to

instability in the target nucleus.

^{7}Li(p,n)^{7}Be The *lowest current* configuration of this reaction—414 μA of 3.8 MeV protons on 0.022 cm target—achieved a truly monoenergetic spectrum, with 94% of the entire neutron flux residing within a 1 MeV energy spread between the 1-2 MeV ROI. The recoil, ^{7}Be, has a very low energy state at 429±0.1 keV. This state reduces the possible energy resolution of the spectrum to ~430 keV, but is inconsequential since the permissible energy spread was set above it at 1 MeV. The target also has only one energy level above ground and below the beam energy. Since this level is only 478 keV, and the cross section for inelastic is quite low, the peak does not divide, though a small amount of divergence is evident. No further improvement of the spectrum is necessary.

3.4.3 Cyclotron Type and System Size

Setting aside the spectral results, we compare the reaction requirements with operating parameters of specific cyclotrons representative of what is commercially available. The cyclotron required for each reaction is dependent on particle type and final energy of the ion beam. The p-^{6}Li, p-^{11}B, and p-^{13}C reactions are discussed separately from the p-^{7}Li reaction.

The p-^{6}Li, p-^{11}B, and p-^{13}C Reactions

The p-^{6}Li reaction requires a 14.5-16.0 MeV proton beam. The CYCLONE 18/9 built by IBA could accommodate those energies. Though designed for 18 MeV protons, the final ion energy in this compact cyclotron can be varied by changing the location of the stripper foil (removes the electron from the hydrogen nucleus, reversing the ion polarity and extracting the beam). With a 1.35 T resistive magnet, the CYCLONE 18/9 is 2.0 m in diameter x 2.2 m high and weighs 25 tons. It may accommodate two

simultaneously extracted beams and operate under 50 kW.[9] Unfortunately, it appears to have a nominal beam current of only 150 μA, which is insufficient for achieving 10^{11} n/s/sr from this reaction. Thus, some development effort would be necessary to design a suitable machine, but such adjustment should be possible.

Both the p-^{11}B and p-^{13}C reaction energetics could be accommodated at the lower 10 MeV range by the CYCLONE 10/5 built by IBA or the TRIUMF 14 built by EBCO TECHNOLOGIES. It is apparent, however, that the higher 12 MeV beam may be more desireable, especially for the ^{11}B reaction. Results of additional simulations not shown above suggest that neutron intensity in the ROI increases for ^{11}B(p,n)^{11}C up to 14 MeV protons. In this case, IBA's self-extracting CYCLONE 14 would be ideal. Its yoke diameter is less than 2 m, and it can deliver up to 2 mA of current with 73% extraction efficiency. Other high intensity machines are the CYCLONE 30 by IBA and the TRIUMF 30 by EBCO; both allow for variable energies down to 15 MeV at 500 μA and 1.25 mA respectively [61, 62].

None of the aforementioned commercial cyclotrons are superconducting. The CYCLONE 30 is designed with a pole radius of 91 cm and average magnetic field of 1 T. The accelerating gradient is 5.25 MV/m. Recall Equation 1.2.5. If the CYCLONE 30 were redesigned with 4 T superconducting magnets to drive protons to a final energy of 14 MeV, the pole radius would decrease to 14 cm. The new accelerating gradient would be 15.9 MeV. Total system size scales by the inverse cube of the magnetic field [63], thus a system analogous in size to the USIC described in section 2.1 is plausible.

There are caveats associated with these accelerator proposals. First, there currently are no commercial-off-the-shelf cyclotrons compatible with the fast neutron imaging reactions described above. Though the CYCLONE 14, CYCLONE 30, and the TRIUMF 30 come close, further development is needed to achieve the specified beam energy and current. Such development would increase lead time and capital cost. Secondly, as mentioned in the previous chapter, compact superconducting cyclotrons are

---

[9]See footnote 1.

not widely available. Thirdly, beam emittance increases in a cyclotron configuration. For instance, the cyclotron publishing the best emittance of the ones mentioned is the TRIUMF 30, with radial emittance of 2π mm·mrad. This is approximately a 2.8 mm diameter beam spot, which is nearly twice that of the RFQ, or less than 3% of its brightness.[10] Some focusing elements of the extracted beam may be required, but decreased brightness is amenable to heat dissipation on the target. The energy spread associated with the emittance in phase space is 1% of the beam energy, or ~1.50 MeV. This spread is significantly greater than that advertised by the LLNL Accsys RFQ ($\sim$250 keV) and would adversely affect the neutron sprectra.

The p-^{7}Li Reaction

The prerequisite beam energy of the p-^{7}Li leaves more room for debate on accelerator choice. Producing 4 MeV protons is well within the capabilities of commercial LINAC providers, but an average current of 414 μA exceeds the off-the-shelf limit and warrants a custom design. By contrast, cyclotrons could be designed to deliver this high current, given the same caveats listed above (non-commercial, development effort, higher emitance, etc). If we consider the development effort needed for each system to be equivalent, then we might compare them by accelerating gradient and power requirements.

A classic cyclotron with an average magnetic field of 1.35 T would have a pole radius of 21 cm. In order to better match commercial RFQ LINAC systems, we choose a final energy of 4.5 MeV. This gives the classic cyclotron an accelerating gradient of 3.3 MV/m.

The power necessary to accelerate the particles from rest to the final energy in a cyclotron is $P = IV$, the beam current times the total voltage imparted to each particle. That would be an ideal system with no losses. A conservative estimate for cyclotron input power is made by assuming a 75% transmission rate and proportional

---

[10]Brightness, $B \approx \eta\, I/\epsilon_{ave}^{2}$, where $\eta = 1/8\pi^{2}$.

factors associated with the CYCLONE 18/9.[11] The corresponding parameters for a more compact superconducting cyclotron are calculated assuming a modest 4 T field. The gradient triples and the input power decreases since the coils will not need to be recharged once loaded.

An RFQ LINAC based on the one proposed by AccSys Technologies to the LLNL team and operating at 173 kW and 425 MHz would be about 2 m long (numbers adjusted to accelerate protons, not deuterons). The accelerating gradient is not significantly less than that of the resistive cyclotron, but much less than the superconducting machine. The pulsed power source consumes unnecessary space and energy. This information is sufficient to use Equation 1.2.3 and match the RFQ's gradient or input power to the superconducting cyclotron, then solve for power and length respectively. Table 3.4 presents the pertinent information to roughly compare the two systems.

Table 3.4: Comparison of classic cyclotron and RFQ LINAC configurations for the p-^{7}Li reaction. While parameters like magnetic field or operating frequency are not fixed and may be optimized in many ways, the order of magnitude difference between the two systems holds true.

	Classic Cyclotron (resistive)	Classic Cyclotron (super-conducting)	RFQ LINAC	RFQ LINAC (to match cyc gradient)	RFQ LINAC (to match cyc power)
B-field (T)	1.35	4.00			
Final energy (MeV)	4.5	4.5	4.5	4.5	4.5
Current (uA)	414	414	414	414	414
Operating frequency (MHz)	4.6	61.4	425	425	425
Vane length or pole radius (m)	0.21	0.07	1.94	0.45	16.79
Accelerating gradient (MV/m)	3.3	9.9	2.3	9.9	0.3
Input power (kW)	35	20	173	742	20

---

[11] The magnet coils draw 15 kW of power in the CYCLONE 18/9. The difference between the peak beam and stand-by load, less the magnet coil load, is 29 kW. That is approximately 8.5 times greater than the ideal $P = IV$ figure. This multiplicative factor is applied to the superconducting case as well.

3.4.4 Target Engineering Issues

So far it has been assumed that, provided the target material is not radioactive or otherwise harmful to humans, a solid target will be less problematic than gaseous deuterium. In reality, impinging any material with 500 μA of protons presents problems of thermodynamics and materials damage. Here we discuss the engineering issues with respect to the different targets of the surviving reactions.

We may assume the target material behaves as a black body in thermal equilibrium: it absorbs all radiation from the particle beam, and then ideally emits all that energy to its surroundings (its emissivity is unity). The total absolute power of energy radiated from the target is given by the Stefan-Boltzmann law:

$$P = A \, \sigma_{SB} \, T^4, \tag{3.4.1}$$

where A is the target surface area, σ_{SB} is the Stefan-Boltzman constant of proportionality (5.67e-8 J/(s·m^2·K^4)), and T is the thermodynamic temperature. We determine the local temperature of the target by considering the power P absorbed to be the target stopping power (in MeV/mm) convolved with the beam current, times its thickness. The beam emittance upon the target gives the surface area of heating. The beam spot radius is assumed to be 1 cm.[12]

Suitable targets must be able to endure the heat shock of the beam without melting or combusting. The target should have high thermal conductivity to remove the added energy. The targets must also be constructible insofar as the pure isotope must be applied at the prescribed thickness to a backing material that is transpar-

---

[12]This is a conservative estimate for the power density transferred from the beam to the target. In actuality the beam is Gaussian shaped in the r-direction, so the heat flux striking the target would be distributed as $p(r) = p_{max} \, exp(-\frac{r^2}{2\sigma^2})$, where σ is the standard deviation of the beam, r is the radius of the beam and p_{max} comes from integrating the exponential in cylindrical coordinates: $p_{max} = \frac{P_{beam}}{2\pi\sigma^2 \left(1 - exp\left(-\frac{R^2}{2\sigma^2}\right)\right)}$. P_{beam} is the beam power ($I \cdot V$), and the full radius of an ion beam R is usually 1.5-2.5 cm. The simplification I employ in this section is to assume P_{beam} exists uniformly for 1 standard deviation, and the heat contribution of the rest of the beam (33%) is neglected.

ent to neutrons, thermally conductive, and structurally able to withstand the flux of uncollided protons. Ideally, the backing material is opaque to protons, stopping their travel without activating and producing unwanted radiation.

Lithium-6 and Lithium-7 Ideal production of monoenergetic neutrons with ^{6}Li involves about 360 μA at 14.5 MeV per proton. That transfers 357 W of power across the thin target, which, using Equation 3.4.1, equates to 2,843 $^\circ$C. The ^{7}Li reaction at 1-2 MeV heats the target to 3,001 $^\circ$C due to the higher current. Lithium has a notoriously low melting point of 180 $^\circ$C and a low thermal conductivity of 85 W/(m·K) at 300 K. Hence, using solid-phase lithium as a target in this high-intensity beam application requires removing power densities of over 3 MW/m^2 in order to prevent phase-change or reaching critical heat flux in the target.

Choice of target is a perennial challenge encountered in the medical field of Boron Neutron Capture Therapy (BNCT).[13] Though some experimental work has been done on water-cooled solid-phase lithium targets, blistering, bubbling and cracks usually forestall a successful design [64]. One technique for removing power densities up to 17 MW/m^2 is submerged jet impingement (Figure 3.4.5, on left). B. Blackburn showed that using liquid gallium as the coolant is advantageous for its exceptional heat transfer coefficient compared to water, allowing for lower nozzle pressures and thinner target backings. He developed a thermohydraulic model for the p-^{7}Li reaction using this technique. The problem with gallium jet cooling is that a target backing is still unavoidable due to the mechanical load of the jet. The backing, the ambient fluid, and the gallium coolant itself will have a neutron cross section that will disturb the fast neutron spectrum. Additionally, the ^{71}Ga isotope captures a neutron to form ^{72}Ga, which releases nine diffrent

---

[13]BNCT relies on a slow neutron source for the activation of ^{10}B injected in the patient; it subsequently alpha decays to ^{7}Li with a Q-value of 2.4 MeV, and both the alpha and recoil nucleus cause ionization in surrounding malignant cells. For a brief overview see www.pharmainfo.net/reviews/boron-neutron-capture-therapy-overview.

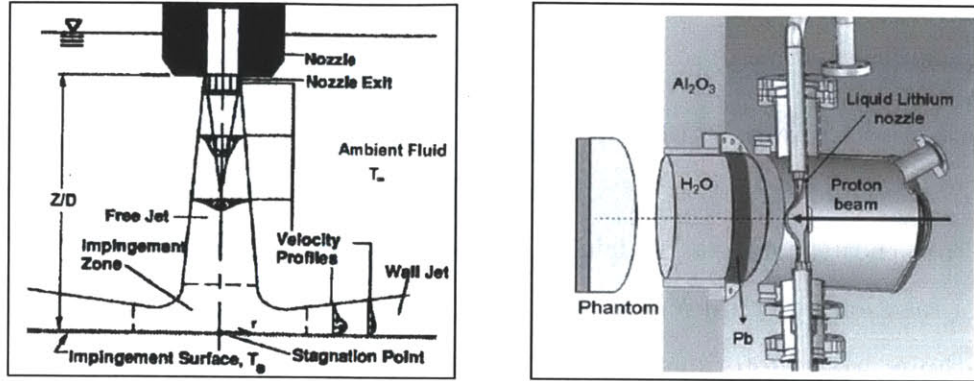gamma rays with intensities over 5% in its decay scheme.

Figure 3.4.5: Submerged jet impingement design for solid-phased Li targets shown on left. Image from [65]. Liquid lithium assembly shown on right, with water moderator [66].

Other applications employing lithium targets resort to a liquid lithium jet, where the ion beam is directed upon a windowless and vacuumed concave wall where the flow is forced from a nozzle. Power is dumped into a containment tank, and the lithium is recirculated back to the nozzle, held at ~200 °C. One prototype developed by Soreq Nuclear Research Center (SNRC) meets the exact specifications of the ^{7}Li reaction discussed here (Figure 3.4.5, on right) [66].

Several complications connected with the liquid lithium target remain. First of all, the liquid-lithium assembly may not be much simpler to implement than the gas-handling subsystem prescribed with the d-D configuration. Lithium is highly reactive, flammable, and oxidizes readily in air. Second, purified ^{6}Li is not commercially available, due to its being a source material for tritium production. Third, the SNRC prototype moderates the ejected neutrons with lead and water or polyethylene. A fast neutron imaging system would not moderate the neutrons, so the uncollided proton exposure to the target backing and other structural materials is a concern. The International Fusion Materials Irradiation Facility (IFMIF) addressed this issue in their ^{7}Li(d,n)^{8}Be operation [67]. Though

IFMIF involves disparate energetics and damage parameters, one sees that the thermo-mechanical and tensile properties of the target backing must still be considered in a liquid lithium jet. Periodic "cut-and-weld" maintenance or use of spectra-flattening ferritic steel components seems inevitable.

In view of the advantages and disadvantages of each design, the liquid lithium is determined to be the most promising for an imaging application. The moderator is not inherent to the design, and a working prototype exists.

Boron-11 and Carbon-13 If the ^{11}B and ^{13}C targets were exposed to the highest currents of Table 3.3, they would reach temperatures around 3,040 and 3,627 $^{\text{o}}$C respectively, which exceeds their corresponding phase transitions of 2,300 and 3,500 $^{\text{o}}$C. The 314 μA ^{11}B configuration decreases the target temperature to 2,724 $^{\text{o}}$C, which is still above melting and sacrifices neutron flux. The 835 μA configuration of ^{13}C reduces the target temperature to 3,534 $^{\text{o}}$C, which is comparable to the melting point and potentially yields more neutrons. In all cases it will still be critical to dissipate the thermal power.

Reduction of thermal power of this magnitude may be acheived with gaseous cooling alone. Another method for handling the heat from high-intensity beams is to decrease their power density by increasing the surface area of exposure. For example, we could apply the target onto a rotating disc. One ADVANCED ENERGY SYSTEMS, Inc. (AES) design is for a 1 μm-thick ^{13}C target continually exposed to 17.6 kW of beam [68]. Employing AES's 12" disc in this application would reduce the total target temperature to 732 $^{\text{o}}$C for ^{11}B and 945 $^{\text{o}}$C for ^{13}C, without water cooling.

Both elements may be sputtered uniformly onto backing substrates at thicknesses of less than 50 μm. Tantalum is an ideal backing for several reasons. It readily forms borides and carbides improving the adhesion and durability of the sputtered layer. It inhibits the formation of bubbles (common in proton beams)

with a good combination of hydrogen solubility and diffusivity. Being high-Z, Ta minimizes gamma production. Finally, it possesses good strength properties in thin stock (e.g. ~0.25 mm) so to be practically transparent to neutrons.

The Ta layer may be braised to a copper disc, and other structural components of the target may be copper, as in the AES design. Copper has high conductivity and favorable performance under thermal stress, though it also has a non-elastic cross section for 9-12 MeV protons around 1 b, and total cross section for 6-11 MeV neutrons around 1.5 b. Some adverse gamma radiation and neutron spectra spreading are expected. It would be advantageous under these beam conditions to utilize GLIDCOP—copper dispersion-strengthened with aluminum oxide—to enhance component strength and resilience to thermal softening and radiation damage.[14]

3.5 Final Discussion

This section synthesizes the preceding observations to provide a final evaluation of the viability of the reactions for fast neutron imaging of the NEP.

3.5.1 Conclusion

The proton reactions on ^{6}Li, ^{11}B, and ^{13}C targets are untenable for fast neutron imaging. The neutron production cross sections for these are sufficient within the limits of reasonable cyclotron energetics and intensities, yet each of these fails due to low-lying energy levels in the target's excitation function. We recall that the detector side of the system seeks incident neutrons with energies different from those of the source, characteristic to the inelastic scatter spectrum associated with the *feature*. Protons

---

[14]GLIDCOP is the registered trademark name of North American Hoganas, Inc. A useful pamphlet on the product is available at www.aps.anl.gov/APS_Engineering_Support_Division/ Mechanical_Operations_and_Maintenance/Miscellaneous/tech_info/Glidcop/ SCM_Glidcop_product_info.pdf.

scattered inelastically in the *source* create multiple peaks and/or a neutron continuum in the spectrum that would be too computationally complex to deconvolute on the detector side.

Recommendation

The p-^{7}Li reaction is an attractive alternative to the d-D reaction. It not only exhibits a monoenergetic spectrum comparable to the d-D reaction in terms of intensity and kurtosis, but it also may produce an even better image. The relative contrast of the neutrons at these lower energies (1-2 MeV) is higher than those in the 6-11 MeV ROI. The total relative contrast of p-^{7}Li, as calculated by Equation 3.2.6, is greater than all of the other reactions, including d-D. These and all other salient aspects of the two configurations are summarized in Table 3.5.

Table 3.5: Summary of current approach and recommendation

	Current Approach	Recommendation
Source reaction	^{2}H(d,n)^{3}He	^{7}Li(p,n)^{7}Be
Accelerator approach	RFQ/LINAC	Superconducting
Projectile energy (MeV)	7.33	3.8
Beam current (uA)	309	414
Input power (kW)	543	20
Operating frequency (MHz)	425	61
Vane length or pole radius (m)	4.83	0.07
Accelerating gradient (MV/m)	1.52	8.64
Accelerator development effort	some: high current	more: high current, new application
Neutron energy (MeV)	10.5	2.1
Neutron ΔE (MeV)	1.4	1.5
Neutron flux (n/s/sr)	10^{11}	10^{11}
Target design	compressed gas w/rotary valve	liquid lithium jet
Target thickness (cm)	4	0.022
Target development effort	more: problematic gas handling system	some: complex design, unwanted radiation
Contaminating radiation	minimal: break-up neutrons	some: gammas from inelastic scatter
Total Relative Contrast[a]	1	3.32

[a] This is a relative figure normalized to the TRC of the d-D configuration; hence, the recommended configuration has an estimated three times better image contrast than the current approach.

The ^{7}Li target would need to be a liquid jet as described above in order to remove thermal power and prevent target destruction. Though lithium oxidizes easily, is highly reactive and flammable, and assembly of a liquid lithium jet system is not simple to implement, such a component is more feasible than the windowless target and deuterium gas handling system. The existence of a working prototype and ample literature and expertise from the BNCT and IFMIF research fields lends greater confidence to the liquid lithium technique.

Additionally, the p-^{7}Li reaction is compatible with a compact cyclotron, which could have operational and cost advantages over the LINAC approach usually taken for beam energies under 4-4.5 MeV. First, both systems would involve equal development effort to accomodate the prerequisite beam intensity. It is uncertain whether this customization is more or less demanding than that being pursued in the existing d-D LINAC approach. Second, the liquid lithium could evaporate under the peak power of the RFQ's pulse. Alleviating this concern would mean reducing the peak power by increasing repetition rate or collection time. The former increases input power; the latter has been fixed in this analysis to allow a fair comparison among all alternatives. The cyclotron's continuous wave gives peak power near the average current. Third, the cyclotron would be much more compact, primarily because the RFQ would be coupled with a klystron. If total system cost is directly proportional to accelerating gradient, the superconducting cyclotron would be more than 4 times more cost effective. If the RFQ was designed according to capital costs fixed to the cyclotron's accelerating gradient, with all other parameters held equal, the operating costs would be over 30 times greater due to the exorbitant input power.

Caveats

Still, there are some caveats to the conclusion that a cyclotron-based p-^{7}Li reaction is a viable alternative for the ESS program. First and foremost, empirical investigation is needed to validate the claim that p-^{7}Li produces a better image than d-D. We rested

this conclusion on the total relative contrast formulation. One suspects statistical limitations of the signal because low-energy neutrons must penetrate a specimen with an absorption cross section monotonically higher in the 1-2 MeV ROI than in the 6-11 MeV ROI. The signal-to-noise formulation (Equation 3.2.7) is the proper way to address the problem, but knowledge of the specimen geometry is necessary. The detector efficiency and intrinsic noise are paramount considerations as well.

Secondly, the p-^{7}Li reaction produces gamma radiation which will interact with the scintillator and contaminate the image. Similarly, the liquid jet target apparatus will activate and produce unwanted radiation. In theory, the windowless d-D target does not posess these drawbacks. Due to simulation impediments previously mentioned, however, the extent of this contamination on the image requires further experimentation.

Thirdly, any cyclotron design described in this analysis would be a first-of-its-kind device. The risks and challenges associated with development of a new device are appreciated, but the unrealized potential of a compact cyclotron demands greater appreciation. The beam energies of the four reactions discussed fall well within the typical range for radioisotope generating cyclotrons, which as a class are becoming ubiquitous with vendors worldwide.[15] The unavailability of the prerequisite currents does not indicate a technological limit but, rather, a market demand condition: high power cyclotrons are not necessary for radiopharmaceutical production. The technology is changing to meet a variety of research and industrial needs. Beam intensity tends to be limited by losses in the extraction foil, imperfect vacuum due to injection systems, and emitance growth due to non-isochronous fields. The success in construction and operation of the CYCLONE 14, CYCLONE 30 (also made by IBA), and TRIUMF 30 by EBCO demonstrates the utility of technical solutions such as modified vacuum

---

[15]According to the DoE, the market for medical particle accelerators exceeds \$3.5 billion per year, and is growing at a rate of more than 10% annually [3]. For a directory of 262 of the expected 350 cyclotrons in use for radionuclide production in 2006 see [69]. For a review of recent accelerator industry growth in Asia with representative vendors and performance parameters of radiopharmaceudical cyclotrons see [70].

pumping systems, integration of high-performance multi-CUSP ion source, and perfect isochronicity to achieve the intensities necessary for fast neutron imaging [71].

On the Method

Finally, a note about the method employed in this examination. A systematic approach was taken in order to survey the possibilities that may have been bypassed when the project team committed to a LINAC configuration for ESS. For the sake of brevity, many details and important possibilities were ignored, casting some doubt on the completeness of the analysis.

The author is given confidence in his method by the fact that all the double-valued reactions listed in [36], less the hazardous and gaseous targets, passed the first sort for energetic compatibility. These reactions have high differential cross sections for neutron production in the forward direction at energies that correlate kinematically with the beam energy.

Second, it is unequivocally observed that to achieve a high specific yield it is necessary to have both a high neutron production cross section and a small energy loss of the projectile in the target. The upper useful projectile energy is determined by the threshold for excitation of the first excited state in the target or recoil nucleus, as several studies state, usually limiting the list of monoenergetic reactions between 1-20 MeV to the "big four": d-D, d-T, p-T, and p-^{7}Li [39, 36, 53, 32, 41, 72]. The fact that p-^{7}Li is the only non-hazardous, non-gaseous target in that group validates our conclusion.

3.5.2 Future Work

Work must continue on the development of the evaluated nuclear database with regard to proton and deuteron reactions in the 1-20 MeV range. There is little if any experimental documentation for these reactions in ENDF. The program TALYS [29]

82

predicts various user-defined outputs utilizing nuclear physics models for target elements above atomic number 12, but is generally unreliable for most engineering efforts. Publications from the IFMIF group stress the importance of proper models for predictive engineering. One paper demonstrates a methodology used to benchmark and refine the Optical Model Potential, which contributes to the possibility of producing quasi-monoenergetic neutrons from recoils of excited target states [73]. The same type of data would be invaluable in further investigation of fast neutron imaging sources.

Could a neutron signal coming from a known specimen be deconvoluted from a multienergetic spectra? The ESS application is unique in that there is a known feature within the specimen. One only is interested in aberrations—aging effects—within that feature. It seems plausible that an algorithm could be developed to correct for continuum neutron contributions to the specimen's characteristic response function. Others mention similar post-processing techniques. M. Drosg discusses background elimination by subtracting a neutron radiograph taken with the background neutrons [36]. J. I. Watterson and J. Guzek develop a computational model that could be used as a precursor [74], which would open up a host of new possibilities. In the present analysis, the p-^{11}B reaction, with its relatively low prerequisite beam current, prominent peaks corresponding to both ROIs, and favorable target conditions, would be an especially attractive solid-phase candidate if non-monoenergetic signal post-processing were possible.

4 Conclusion

This thesis discussed three potential applications of compact cyclotrons: generation of ^{13}N for PET imaging, active interrogation for counter-proliferation, and fast neutron imaging of the nuclear explosive package. For brevity, each application was covered broadly, with limited emphasis on details. I hesitated to take this approach, yet, three common themes emerged that may have been missed if a narrower, more in-depth study of a single application was chosen.

First, the accelerating gradient—final ion energy divided by path length—is the single most salient characteristic leading to the marketability of cyclotrons. It is remarkable how much advancement could occur simply by careful application of the Lorentz Force Law. I say this with an appreciation of betatron oscillations, space charge, Twiss parameters and tune resonances, etc, all making cyclotrons a quite challenging tool to work with sometimes. Resistive compact cyclotrons are already profitable in the medical industry primarily because they have a smaller footprint than their LINAC competitors. Not only are capital costs proportional to the length of the machine, but ever smaller machines may be more profitable because they open up new markets and economies of scale. The move to superconducting coils increases the gradient to 2-4 times that of a LINAC and reduces the input power significantly (though superconductors do bring a new set of physical laws to bear since the device must be held near 4 K). This disparity crystallized with the comparison of different accelerator configurations for the p-^{7}Li reaction in Section 3.4.3. In that analysis, were it not for superconducting cyclotrons, the RFQ LINAC would be the obvious tool for the task.

The accelerating gradient must be the factor that motivates further development of cyclotrons to make them more compact, with better extraction rates, driving beams of less emittance and higher power.

Second, compact cyclotrons change the way we approach a problem. The accelerating gradient opens up altogether new possibilities, like new reactions in fast neutron imaging, new economics in radiopharmaceuticals, and new mission sets in counter-proliferation. Only marginal benefits could be expected by simply retooling old methods in the PET production and counter-proliferation fields. In the ESS solution proposed by LLNL, it seems like a problematic system was designed to fit the accelerator. An objective, fresh perspective was necessary. In turn, Chapter 3 was less a study on fast neutron imaging than it was an example of systematically bringing a new paradigm to the drawing board.

Third, it is unlikely that compact cyclotrons will transform a field all at once; it will be a gradual rippling effect. A user's accelerator choice is linked to other technologies, systems, and institutions bearing on the problem. These bodies of knowledge and patterns of thinking or doing business must catch up to the possibilities of the new technology. The recurring example from this thesis is the lack of evaluated data files or reliable physics models for light ion interactions. Complete ENDF databases would be an invaluable resource for simulations and preliminary engineering of cyclotron applications, as they are for high energy physics and criticality research, but it will take time for publicly and privately funded institutions to see the value in such work and prioritize their time accordingly. Another example from the PET production case is that a successful ^{13}N product does not guarantee market access. Stringent quality control measures regulate radiopharmaceuticals, and not only have ^{99}Mo/^{99m}Tc suppliers already adjusted their products and processes to maximize profits, they thrived in the market as the regulations were formed. This is a major barrier to market entry for PET isotope suppliers, one that may not be economically balanced by the cyclotron system size and power advantages alone. Public institutions may need to subsidize

manufacturing of ^{13}N, and other alternatives to HEU-derived SPECT isotopes, in order to capture the collective benefit of improved nuclear security they afford. Similar arguments could be made for other cyclotron applications, which is the premise of the DOE report quoted earlier [3].

One final word should be mentioned on the potential for undesirable uses of compact cyclotrons. The breeding of radioisotopes is not too far removed from the breeding of fissile material from fertile material. In this way accelerators become a proliferation pathway. One study found that this would be a very difficult and costly undertaking, comparable to the construction of a small plutonium production reactor. The difference is that accelerators or their facilities are not regulated by the IAEA or international export controls. A would-be proliferator may choose to acquire SNM through electronuclear breeding simply because it is *not* a reactor [75].

The pace of international technology diffusion, promoted in a way even by this thesis, should cause concern and motivate preventative action. There is a large amount of accelerator-based transmutation information published in open literature from the related field of nuclear waste disposal. Commercial turn-key systems can be ordered and shipped with no regulator interference. Currently, the prospects of electronuclear breeding are limited because most commercial systems are low current. As discussed, however, cyclotrons are trending toward being more compact and higher powered to meet industry demands. In view of this, private companies should report to the government all exports of accelerators and accelerator-related technical knowledge, and intelligence activities should include sensing for the signatures of electronuclear breeding.

Bibliography

[1] (2012) Lawrence and the Cyclotron. American Institute of Physics, Center for History of Physics. [Online]. Available: http://www.aip.org/history/lawrence/

[2] W. K. H. Panofsky. (1997) The Evolution of Particle Accelerators and Colliders. US Department of Energy, National Accelerator Laboratory (SLAC). Menlo Park, CA. [Online]. Available: http://www.slac.stanford.edu/pubs/beamline/27/1/27-1-panofsky.pdf

[3] US Department of Energy, "Accelerators for America's Future." June 2010.

[4] J. C. Slater, "The Design of Linear Accelerators," Massachusetts Institute of Technology, Research Laboratory of Electronics, Tech. Rep. 47, September 1947.

[5] S. Livingston, *Particle Accelerators*. McGraw-Hill, 1962, ch. 10, pp. 310–348.

[6] R. H. Stokes and T. P. Wangler, "Radiofrequency Quadrupole Accelerators and their Applications," *Annual Review Nuclear Particle Science*, vol. 38, pp. 97–118, 1988.

[7] B. Rusnak, J. Hall, P. Fitsos, J. Sain, R. Souza, and S. Anderson, "Technology Approach for Neutron Imaging: Overall Technical and Cost Review," Lawrence Livermore National Laboratory, Tech. Rep. LLNL-PRES-523916, February 2012.

[8] S. Humphries Jr., *Principles of Charged Particle Acceleration*. Albuquerque, NM: John Wiley and Sons, 1999.

[9] Y. G. Alenitsky *et al.*, "Isochronous Cyclotron C250 for Proton Therapy Application," in *Proceedings of RuPAC*, Zvenigorod, Russia, 2008, pp. 342–344.

[10] X. F. Shen, M. de Jong *et al.*, "Status and Upgrade Plan of 250 Mev LINAC at CLS," in *Proceedings of LINAC08*, Victoria, BC, Canada, 2008, pp. 380–382.

[11] T. Antaya, "Comprehensive Introduction to Cyclotron Science and Technology: Superconducting Magnet Technologies for Cyclotrons," Class Lecture, Massachusetts Institute of Technology, Cambridge, 2011.

[12] F. J. Bonte, T. S. Harris *et al.*, "Tc-99m HMPAO SPECT in the Differential Diagnosis of the Dementias with Histopathologic Confirmation," *Clinical Nuclear Medicine*, vol. 31, no. 7, pp. 376–378, July 2006.

[13] A. Elhendy, J. J. Bax, and D. Poldermans, "Dobutamine Stress Myocardial Perfusion Imaging in Coronary Artery Disease," *Journal of Nuclear Medicine*, vol. 43, no. 12, pp. 1634–1646, December 2002.

[14] (2009) NRC Committee on Medical Isotope Production Without Highly Enriched Uranium: Medical Isotope Production without Highly Enriched Uranium. National Research Council / National Academy of Sciences. Washington DC. [Online]. Available: http://www.nap.edu/openbook.php?record_id=12569&page=R1

[15] D. Ljunggren. (2007, December) Canadian Parliament Orders Isotope Reactor Restart. Reuters. Ottawa, Canada. [Online]. Available: http://www.reuters.com/article/2007/12/13/us-cancer-idUSN1154689120071213

[16] (2009, July) Reliable Domestic and Global Supplier of Molybdenum-99 (Mo-99) and Switch from Highly Enriched Uranium (HEU) to Low-Enriched Uranium (LEU) to Produce Mo-99. Coalition of Professional

Organizations. [Online]. Available: http://interactive.snm.org/docs/Isotope% 20White%20Paper%20Final_July%202009.pdf

[17] (2011, June) Record Levels of Non-HEU-Based Mo-99 Supplied to the United States. NNSA. [Online]. Available: http://nnsa.energy.gov/mediaroom/ pressreleases/nonheumo996211

[18] (2012, November) A Review of the Supply of Molybdenum-99, the Impact of Recent Shortages and the Implications for Nuclear Medicine Services in the UK. Administration of Radioactive Substances Advisory Committee. [Online]. Available: http://www.oecd-nea.org/med-radio/docs/ ARSACStrategicReport99Mo-99mTcfinalv2HQ.pdf

[19] D. L. Bailey, D. Townsend, P. Valk, and M. Maisey, Eds., *Positron Emission Tomography*, 3rd ed. Basic Sciences, 2005.

[20] S. Takacs *et al.*, "Validation and Upgrading of the Recommended Cross Section Data of Charged Particle Reactions Used for Production of PET Radioisotopes," *Nuclear Instruments and Methods in Physics Research B*, vol. 211, pp. 169–189, 2003.

[21] "Radiation Dose to Patients from Radiopharmaceuticals," Annals of the ICRP, New York, Tech. Rep. Publication 53, 1988.

[22] J. Kiener *et al.*, "Gamma-ray Production by Inelastic Proton Scattering on O-16 and C-12," *Physical Review C*, vol. 58, no. 4, pp. 2174–2179, 1998.

[23] A. Gholamrezanezhad and G. Mariani, "Future of Nuclear Medicine: SPECT Versus PET," *The Journal of Nuclear Medicine*, vol. 50, no. 7, pp. 16N–18N, July 2009.

[24] R. Krasikova *et al.*, "Improved N-13 Ammonia Yield from the Proton Irradiation

of Water Using Methane Gas," *Applied Radiation and Isotopes*, vol. 51, pp. 395–401, 1999.

[25] R. Lanza, "Detecting Fissile Materials," Class Lecture, 22.814, Massachusetts Institute of Technology, Cambridge, October 2011.

[26] J. T. Mihalczo, "Radiation Detection for Active Interrogation of HEU," U.S. Department of Energy, Oak Ridge, TN, Tech. Rep. ORNL/TM-2004/302, December 2004.

[27] T. N. Taddeucci and R. L. Sheffield, "Neutron and Gamma-ray Production with Low Energy Beams," Los Alamos National Lab, Tech. Rep. LA-UR-07-2724, April 2007.

[28] R. Lanza, "Accelerator-Based Techniques for Detection of Explosives and SNM," in *Neutron Based Techniques for the Detection of Illicit Materials and Explosives*. Johannesburg, South Africa: IAEA RCM, November 2009.

[29] (2011) TALYS Nuclear Reaction Simulation Software. NRG. Petten, Netherlands. Version 1.4.

[30] G. F. Knoll, *Radiation Detection and Measurement*, 4th ed. John Wiley and Sons, 2010, ch. 3, pp. 65–99.

[31] L. De Geer, "Nonintrusive Detection of Nuclear Weapons on Ships," *National Defense Research Establishment*, February 1990.

[32] "Neutron Imaging: A Non-Destructive Tool for Materials Testing," IAEA, Vienna, Tech. Rep. IAEA-TECDOC-1604, September 2008, Report of a coordinated research project.

[33] (1995, May) The Stockpile Stewardship and Management Program: Maintaining Confidence in the Safety and Reliability of the Enduring U.S. Nuclear Weapon

Stockpile. US Department of Energy, Office of Defense Programs. [Online]. Available: http://www.fas.org/nuke/guide/usa/doctrine/doe

[34] K. Walter. (1998, January) Enhanced Surveillance of Aging Weapons. Lawrence Livermore National Lab. [Online]. Available: https://www.llnl.gov/str/Kolb.html

[35] J. Hall, B. Rusnak *et al.*, "Physics and Experimental Basis for Neutron Imaging: Overall Technical and Cost Review," Lawrence Livermore National Laboratory, Tech. Rep., February 2012.

[36] M. Drosg. (2009, 30 August) Characteristics of Accelerator-Based Neutron Sources. University of Vienna. Wien, Austria. [Online]. Available: http://homepage.univie.ac.at/manfred.drosg/indexen.htm

[37] M. Drosg. (2000, January) DROSG-2000. Documented in the IAEA Report IAEA-NDS-87 Rev. 5.

[38] J. Sain, J. Hall, B. Rusnak, and P. Fitsos, "Optical Imaging System for High-Energy Neutron Imaging," Technical and Cost Review, Lawrence Livermore National Laboratory, Tech. Rep., Feb 2012, lLNL-PRES-525151.

[39] R. M. Ambrosi, "A Model for the Physics of Image Formation in Fast Neutron Radiography," Ph.D. dissertation, University of the Witwatersrand, Johannesburg, 2000.

[40] G. F. Knoll, *Radiation Detection and Measurement*, 4th ed. John Wiley and Sons, 2010, ch. 8, pp. 223–275.

[41] R. Nolte and D. J. Thomas, "Monoenergetic Fast Neutron Reference Fields: I. Neutron Production," *Metrologia*, vol. 48, pp. S263–S273, 2011.

[42] B. Ruznak, Personal Communication, Feb 2012.

[43] B. Pritychenko and A. Sonzogni. Q-value Calculator. Brookhaven National Laboratory, National Nuclear Data Center. [Online]. Available: www.nndc.bnl. gov/qcalc/

[44] G. F. Knoll, *Radiation Detection and Measurement*, 4th ed. John Wiley and Sons, 2010, ch. 15, pp. 553–595.

[45] W. Catford. (2004, January) Catkin 2.02. Kinematics Spreadsheet.

[46] "Investigation of the N-15(p,n) Reaction for Use as a Neutron Source in Scattering Experiments," in *Fast Neutron Detectors and Applications Conference*, vol. 059, 2006.

[47] M. Cosack, H. Lesiecki, and J. B. Hunt, "Monoenergetic Neutrons from the Sc-45(p,n)Ti-45 Reaction," IAEA, Vienna, IAEA Report IAEA-TECDOC-0410, 1987.

[48] J. H. Gibbons, R. L. Macklin, and H. W. Schmitt, "V-51(p,n)Cr-51 Reaction as a 5- to 120-keV Neutron Source," *Physical Review*, vol. 100, pp. 167–8, 1955.

[49] "MCNPX (TM) – A General Monte Carlo N-Particle Transport Code, Version 5," Los Alamos National Laboratory, 2008.

[50] J. Hall, Personal Communication, Mar 2012.

[51] G. F. Knoll, *Radiation Detection and Measurement*, 4th ed. John Wiley and Sons, 2010, ch. 2, pp. 29–56.

[52] N. Tsoulfanidis, *Measurement and Detection of Radiation*, 3rd ed. CRC Press, 2011.

[53] D. T. L. Jones, "Monoenergetic Neutron Sources Below 100 MeV," *Radiation Physics and Chemistry*, vol. 61, pp. 469–472, 2001.

[54] L. S. Waters, *MCNPX User's Manual, Version 2.3.0*, Los Alamos National Laboratory, April 2002.

[55] B. Wakefield and B. Macefield, "A Study of the Li-6(p,n)Be-6 Reaction," *Nuclear Physics A.*, vol. A114, pp. 561–576, 1968.

[56] F. Petrovich *et al.*, "Nucleon Scattering from Light Nuclei," *Nuclear Physics A.*, vol. A383, pp. 355–391, 1982.

[57] W. von Witsch, G. S. Mutchler, and D. Miljanic, "Isospin Purity of the 5.37 MeV State in Li-6," *Nuclear Physics A.*, vol. A248, pp. 485–495, 1975.

[58] C. P. Browne and H. Stocker, "Additional Accurate Excitation Energies of B-11," *Physical Review C*, vol. 4, pp. 1481–1482, 1971.

[59] S. M. Grimes *et al.*, "Gamow-Teller Matrix Elements from the B-11(p,n)C-11 Reaction," *Physical Review C*, vol. 31, pp. 1679–1690, 1985.

[60] G. Rickards, B. E. Bonner, and G. C. Phillips, "Measurement of (p,n) Thresholds at Tandem Energies," *Nuclear Physics*, vol. 86, pp. 167–186, 1966.

[61] S. Lucas *et al.*, "Current Performance of the Self-extracting Cyclotron," in *AIP Conference Proceedings*, vol. 680, no. 956. American Institute of Physics, 2003.

[62] T. Kuo *et al.*, "Review on Beam Characteristics of High Current H- Cyclotrons," in *18th International Conference on Cyclotrons and their Applications*, Giardini, Naxos, November 2007.

[63] T. Antaya, "Comprehensive Introduction to Cyclotron Science and Technology: Compact Superconducting Cyclotrons," Class Lecture, Massachusetts Institute of Technology, Cambridge, 2011.

[64] E. Forton *et al.*, "Overview of the IBA Accelerator-based BNCT System," *Applied Radiation and Isotopes*, vol. 67, pp. S262–S265, July 2009.

[65] B. Blackburn, "High-Power Target development for Accelerator-Based Neutron Capture Therapy," Ph.D. dissertation, Massachusetts Institute of Technology, February 2002.

[66] S. Halfon, M. Paul, A. Arenshtam, and D. Berkovits, "High-power Liquid-lithium Target Prototype for Accelerator-based Boron Neutron Capture Therapy," *Applied Radiation and Isotopes*, vol. 69, no. 12, pp. 1654–1656, December 2011.

[67] B. Riccardi, S. Roccella, and G. Micciche, "IFMIF Lithium Target Backplate Design Integration and Thermo-mechanical Analysis," *Fusion Engineering and Design*, vol. 82, pp. 2518–2523, 2007.

[68] J. Rathke and E. Peterson, "Engineering Design of a Continuous Duty gamma-production Proton Target for the Contraband Detection System," in *Proceedings of the 1999 Particle Accelerator Conference*, New York, 1999.

[69] "Directory of Cyclotrons Used for Radionuclide Production in Member States: 2006 Update," IAEA, Vienna, Tech. Rep. IAEA-DCRP/2006, October 2006.

[70] C. Tang, "Present Status of the Accelerator Industry in Asia," in *Proceedings of International Particle Accelerator Conference*, 2010, pp. 2447–2451.

[71] A. I. Papash and Y. G. Alenitsky, "On Beam Intensity Upgrade in the Commercial Cyclotrons of Negative Hydrogen Ions," *Physics of Particles and Nuclei Letters*, vol. 5, no. 5, pp. 469–472, 2008.

[72] C. A. Uttley, "Sources of Monoenergetic Neutrons," in *Neutron Sources for Basic Physics and Applications*, S. Cierjacks, Ed. Oxford, UK: Pergamon Press Ltd., 1983, pp. 19–55.

[73] U. Fischer *et al.*, "Evaluation and Validation of d-Li Cross Section Data for the IFMIF Neutron Source Term Simulation," *Journal of Nuclear Materials*, vol. 367-370, pp. 1531–1536, 2007.

[74] J. I. W. Watterson and J. Guzek, "The Development of a Computational Model for Fast Neutron Radiography," in *Proceedings of SPIE 2867*, vol. 358. Crete, Greece: International Conference on Neutrons in Research and Industry, June 1996.

[75] S. Kemp, "Nuclear Proliferation with Particle Accelerators," *Science and Global Security*, vol. 13, pp. 183–207, 2005.